

# INVESTIGATION OF PRISTINE AND OXIDIZED POROUS SILICON

*ANDREA EDIT  
PAP*

Faculty of Technology,  
Department of Electrical and  
Information Engineering,  
Infotech Oulu,  
University of Oulu

OULU 2005





**ANDREA EDIT PAP**

**INVESTIGATION OF PRISTINE AND  
OXIDIZED POROUS SILICON**

Academic Dissertation to be presented with the assent of  
the Faculty of Technology, University of Oulu, for public  
discussion in Raahensali (Auditorium L10), Linnanmaa,  
on July 1st, 2005, at 12 noon

OULUN YLIOPISTO, OULU 2005

Copyright © 2005  
University of Oulu, 2005

Supervised by  
Professor Seppo Leppävuori

Reviewed by  
Professor Reino Laiho  
Professor Turkka Tuomi

ISBN 951-42-7774-0 (nid.)  
ISBN 951-42-7775-9 (PDF) <http://herkules.oulu.fi/isbn9514277759/>  
ISSN 0355-3213 <http://herkules.oulu.fi/issn03553213/>

OULU UNIVERSITY PRESS  
OULU 2005

## **Pap, Andrea Edit, Investigation of pristine and oxidized porous silicon**

Faculty of Technology, University of Oulu, P.O.Box 4000, FIN-90014 University of Oulu, Finland,  
Department of Electrical and Information Engineering, Infotech Oulu, University of Oulu, P.O.Box  
4500, FIN-90014 University of Oulu, Finland  
2005  
Oulu, Finland

### ***Abstract***

While numerous publications deal with the properties and applications of porous silicon (PS), some of the related topics are not complete or could be investigated from different aspects. Therefore, the main objective of this thesis is to provide novel information associated with the optical and chemical properties of PS.

For the investigations, various PS samples are manufactured by electrochemical dark etching of boron-doped p<sup>+</sup>-type Si wafers. Amongst others, (i) the wavelength-dependent refractive indices of freestanding PS monolayers having different porosities were obtained from optical transmission and reflection spectra in the 700–1700 nm wavelength range, and compared to those calculated from Bruggeman's effective medium approximation (EMA). The refractive indices of the PS samples are shown to be described well with the EMA. In addition, optical scattering at the air-PS interface was demonstrated. (ii) Multilayer stacks are created by alternating the porosities of PS layers within the same sample to form Bragg filters. The Bragg conditions of the filters are calculated and compared to optical transmission measurements. (iii) The oxidation of PS membranes in dry air is investigated with emphases on the reaction kinetics and on the structural changes of the porous matter. As revealed, oxidation proceeds faster in PS than in Si bulk. The formed SiO<sub>2</sub> is amorphous and causes stress in the lattice of the residual Si skeleton. (iv) The effect of oxidation extent of PS layers on the growth mechanism of multi-walled carbon nanotubes (CNTs) is investigated. The density of the CNT network is found proportional to the oxidation extent of the substrates. (v) Finally, the chemically-reductive nature of PS is studied and exploited via the immersion plating method to deposit palladium and silver nanoparticles in the nanopores and on the surface of PS samples.

The presented novel results have potential in silicon-based technologies, including integrated active and passive optical components (waveguides, filters, antireflection coatings, optical gas/liquid sensors), electronic devices (electrochemical gas/liquid sensors, diodes, field effect devices) and selective chemical catalysis (substrates, growth templates).

*Keywords:* Bragg grating, chemical catalysis, CNT growth, dry thermal oxidation, EMA, metallization, reaction kinetics, refractive index



## Acknowledgments

First of all, I wish to thank my supervisor Professor Seppo Leppävuori for his support and attention during my studies and research work. I would like to express my gratitude to Professor Jouko Vähäkangas and Professor Heli Jantunen for their continuous and helpful support of my study. I am very grateful to Dr. Krisztián Kordás, the tutor of my studies, for his encouragement, help and patience.

I also want to acknowledge Professor Thomas F. George (University of Missouri, St. Louis, USA), Docent Antti Uusimäki, M.Sc. Géza Tóth and Lich. Tech. Juhani Levoska for fruitful discussions, and for their contribution to the progress of this thesis. Special thanks for everyone in the Microelectronics and Materials Physics Laboratories for their co-operation, technical assistance, and valuable contribution to my work and to the pleasant working atmosphere. The assistance from the staff of the Institute of Electron Optics, and the Electronics Laboratory, Department of Information and Electrical Engineering, University of Oulu is also acknowledged.

I would like to thank Professor Reino Laiho and Professor Turkka Tuomi for reviewing and commenting on the thesis.

This study has been accomplished at the Microelectronics and Materials Physics Laboratories during the years 2002-2005. The work was financially supported by the EMPART Research Group of the Infotech Oulu, the Academy of Finland, Tauno Tönning Säätiö, Oulu University Foundation, Tekniikan Edistämissäätiö and Naisten Tiedesäätiö, all of which are gratefully acknowledged.

Oulu, April 2005

Andrea Edit Pap



## List of symbols and abbreviations

AFM	atomic force microscopy
CCVD	catalytic chemical vapor deposition
CL	cathodoluminescence
CNT	carbon nanotube
CVD	chemical vapor deposition
EDX	energy dispersive X-ray analysis
EFTEM	energy filtered transmission electron microscopy
EL	electroluminescence
EMA	effective medium approximation
FED	field emission device
FEM	finite-element method
FESEM	field emission scanning electron microscopy
FIPOS	full isolation by porous oxidized silicon
IPOS	isolation by porous oxidized silicon
IR	infrared
ITO	indium tin oxide
IUPAC	International Union of Pure and Applied Chemistry
LED	light emitting diode
MEMS	microelectromechanical system
OSA	optical spectrum analyzer
MWCNT	multi-walled carbon nanotube
PD	photodiode
PL	photoluminescence
PS	porous silicon
RSD	relative standard deviation
SEM	scanning electron microscopy
SIKO	silizium kondensator (silicon capacitor)
SOI	silicon-on-insulator
STM	scanning tunneling microscopy
UV	ultraviolet
XRD	X-ray diffraction



## List of original papers

The thesis is based on the following seven papers, which are referred in the text by their Roman numerals.

- I Kordás K, Pap AE, Beke S & Leppävuori S (2003) Optical properties of porous silicon. Part I: Fabrication and investigation of single layer. *Optical Materials* 25: 251-255.
- II Kordás K, Beke S, Pap AE, Uusimäki A & Leppävuori S (2003) Optical properties of porous silicon. Part II: Fabrication and investigation of multilayer structures. *Optical Materials* 25: 257-260.
- III Pap AE, Kordás K, Vähäkangas J, Uusimäki A, Leppävuori S, Pilon L & Szatmári S (2005) Optical properties of porous silicon. Part III: Comparison of experimental and theoretical results. *Optical Materials*, in press.
- IV Pap AE, Kordás K, Tóth G, Levoska J, Uusimäki A, Vähäkangas J, Leppävuori S & George TF (2005) Thermal oxidation of porous silicon: Study on structure. *Applied Physics Letters* 86: 041501.
- V Pap AE, Kordás K, George TF & Leppävuori S (2004) Thermal oxidation of porous silicon: Study on reaction kinetics. *Journal of Physical Chemistry B* 108: 12477-12474.
- VI Kordás K, Pap AE, Vähäkangas J, Uusimäki A & Leppävuori S (2005) Carbon nanotube synthesis on oxidized porous silicon. *Applied Surface Science*, in press.
- VII Pap AE, Kordás K, Peura R & Leppävuori S (2002) Simultaneous chemical silver and palladium deposition on porous silicon; FSEM, TEM, EDX and XRD investigation. *Applied Surface Science* 201: 56-60.

The research work presented in this thesis is divided into three parts. The first includes the original Papers I, II and III and reports on the optical properties of pristine PS single- and multilayers. The second discusses the investigation of low temperature dry thermal oxidation of PS. The results obtained from the reaction kinetics and from the structural changes in the matter are published in Papers IV and V. The third, which is the final part of the thesis, deals with some selected applications of both pristine and oxidized PS. In

Papers II and III, multilayer PS stacks functioning as Bragg gratings are designed and demonstrated. Furthermore, in Paper III, antireflection layers on freestanding PS samples are presented. In paper VI, CNT synthesis on pristine and oxidized PS surfaces, along with the effect of different oxide content on the growth rate, are investigated. Finally, the deposition of Pd and Ag nanoparticles in the pores and on the surface of PS is demonstrated in Paper VII.

Most of the experimental work was accomplished by the author of this thesis. The interpretation of the experimental results and calculations were done in collaboration with the co-authors. The manuscripts of Papers III, IV, V and VII were written by the author of this thesis.

The experimental work was executed mainly in the Microelectronics and Materials Physics Laboratories, Department of Electrical and Information Engineering, University of Oulu. The optical transmission and reflection spectra were recorded in the Electronics Laboratory, Department of Electrical and Information Engineering, University of Oulu. The SEM, FESEM, EFTEM/EDX and part of the XRD analyses were accomplished in the Institute of Electron Optics, University of Oulu. The synthesis of CNTs was carried out in the Materials Research Center, Department of Materials Science Engineering, Rensselaer Polytechnic Institute, Troy, USA.

# Contents

Abstract	
Acknowledgments	
List of symbols and abbreviations	
List of original papers	
Contents	
1 Introduction .....	13
1.1 Overview .....	13
1.2 Objective and outline of the thesis.....	15
2 Synthesis and properties of porous silicon .....	16
2.1 Fabrication of porous silicon by electrochemical etching .....	16
2.2 Mechanism of silicon dissolution and pore formation.....	18
2.3 Key features of porous silicon layers.....	22
2.4 Chemical properties of porous silicon .....	22
2.5 Physical properties of porous silicon.....	24
2.6 Applications of porous silicon .....	26
3 Experimental methods .....	28
3.1 Porous silicon synthesis and characterization.....	28
3.2 Optical measurements.....	31
3.3 Dry thermal oxidation.....	32
3.4 Carbon nanotube synthesis .....	32
3.5 Simultaneous chemical silver and palladium deposition .....	32
3.6 Analyses and measurements .....	33
4 Results and discussion.....	34
4.1 Optical properties of porous silicon.....	34
4.1.1 Study on layers of uniform porosities.....	34
4.1.2 Investigation of layers with alternating porosities .....	38
4.2 Dry thermal oxidation of porous silicon .....	41
4.2.1 Study on structure.....	41
4.2.2 Study on reaction kinetics.....	45

4.3 Some applications of porous silicon .....	48
4.3.1 Optical applications .....	48
4.3.2 Carbon nanotube synthesis on porous silicon.....	48
4.3.3 Silver and palladium deposition on porous silicon for a novel catalyst.....	50
5 Conclusions .....	53
References	

# 1 Introduction

## 1.1 Overview

Porous silicon can be considered as a silicon crystal having a network of voids in it. The nanosized voids in the Si bulk result in a sponge-like structure of pores and channels surrounded with a skeleton of crystalline Si nanowires. The physical properties of porous silicon are fundamentally determined by the shape and diameter of pores, the thickness and the relative content of Si, voids, and in some cases, the relative content of different Si compounds in the formed porous layer. These parameters depend on preparation conditions, so that it is possible to design materials with physical properties of those between Si and air (or the medium which fills the pores). In addition, when the feature size of the Si wires is less than a few nanometers, various quantum-size effects occur which make PS even more fascinating. Because of its versatility and tunable/designable characteristics, PS has become a popular material among scientists and technologists, and has been applied in various fields during the past two decades.

The first PS structure was introduced by Arthur Uhlir in 1956, but contemporaries showed low-level interest in this subject, and it has not changed substantially until the beginning of the 1990s. In 1971, Watanabe and Sakai demonstrated the first application of PS in electronics, the so-called full isolation by the porous oxidized Si process (FIPOS), where the PS layers were used for device isolation in integrated circuits. In the 1980's, the silicon-on-insulator (SOI) in integrated circuits technology (Takai & Itoh 1982), the silicon on sapphire technology (SOS), and silicidation of porous silicon (Ito *et al.* 1989) were introduced as well. Pickering *et al.* have observed low temperature photoluminescence already in 1984. The discovery of room-temperature photo- and electroluminescence by Leigh Canham in 1990, boosted up the research because of the huge potential in silicon-based integrated optoelectronics applications. In a few years, the number of publications significantly increased, where the papers were dealing not only with the manufacturing processes but with the physical and chemical properties, and different applications of PS. The material was found applicable in the areas of electronics, optics, sensors, etc.

A disadvantage of this material is the aging, i.e., the slow spontaneous oxidation of PS. In 1965, Beckmann observed that during a longer storage time period in ambient air, the created PS film became oxidized. This chemical conversion is slow and basically similar to the aging of Si wafers (Harrison & Dimitriev 1991) i.e. a native oxide layer forms on the surface of pores. Due to the ageing effect, the structural (Astrova *et al.* 2002) and optical properties (Karacali *et al.* 2003) of PS show continuous change with the storage time. The growth of the native oxide is completed approximately after a year (Petrova *et al.* 2000). In order to avoid the transient period of aging, various oxidation processes were proposed to oxidize/passivate the PS structures (Rossi *et al.* 2001, Maiello *et al.* 1997). Chemical, anodic, dry and wet thermal oxidation processes have been investigated and presented in these works to eliminate the aging problem. Both the partial oxidation (pre-oxidation) and the full oxidation procedures are used in optical applications, such as optical waveguides, photodetectors, dielectric filters and photoluminescent components.

The topics related to PS represent still a progressive research area (Fig. 1) with a wide range of novel ideas and applications such as biological sensors based on functionalized PS substrates (Dzhafarov *et al.* 2001 and DeLouise & Miller 2004), electrolyte-insulator-semiconductor capacitor (EISCAP) based on silicon and PS for detecting different organic materials, selective chemical sensors/catalysts (Sailor 1997 and Mannion 2004), integrated light-emitting devices on silicon chips (Bondarenko & Yakovtseva 1997 and Nakajima *et al.* 2004), piezoresistive pressure sensors (Pramanik *et al.* 2005), solar cells (Menna & Tsuo 1997 and Aroutiouian *et al.* 2004), etc.

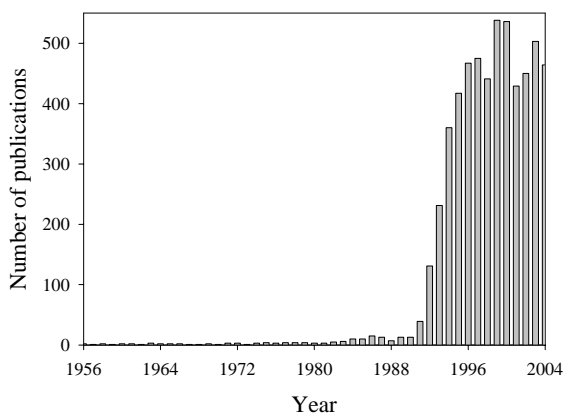


**Fig. 1. Number of publications in refereed journals dealing with porous silicon. (The data are based on the search for the keywords “porous silicon” for a particular year using the search engine of Thomson ISI.)**

## 1.2 Objective and outline of the thesis

The main objective of this thesis is to provide information associated with the optical and chemical properties of porous silicon (PS) needed to accomplish novel applications. Therefore, the wavelength dependent refractive index for PS layers of different porosities in the visible and in the near-IR range are measured and discussed; and the reaction kinetics of PS oxidation in air and its effect on the materials structure are investigated.

Chapters 1 and 2 deal with a short literature overview of the research on PS since its discovery and introduce the state-of-the-art in the synthesis, properties and applications of PS. In Chapter 3, the experimental procedures for synthesizing and modifying single and multilayer PS structures are described. The details of optical transmission/reflection measurements on both supported and freestanding PS films are introduced. This is followed by the technical details of PS oxidation in dry air. Next, the experiments for growing carbon nanotubes on the oxidized PS samples are presented, followed by the details of metal nanoparticle deposition on PS films. The chapter ends with a list of the instrumentation used in the experimental work.

In Chapter 4.1-4.3, the experimental observations, calculations and explanations of the findings, together with a short theoretical background, are discussed. First, the refractive indices of PS monolayers having different porosities are computed from the recorded transmission and reflection spectra, and the results are compared to the refractive indices obtained from calculations based on Bruggeman's effective medium approximation (EMA). Light scattering at the air-PS interface is demonstrated and its effect on the recorded optical spectra are shown (Paper I and III). Furthermore, the transmission bands and Bragg conditions of PS multilayer stacks are investigated and calculated (Paper II and III). Since the optical properties depend on the presence and value of the chemical component, especially the oxidation extent of the PS layer, the procedure often used for the aging effect elimination is the oxidation of the PS structure. Therefore, dry thermal oxidation of PS is investigated and discussed with emphasis on the chemical reaction kinetics and on the structural changes in the porous matter (Papers IV and V).

In Chapter 4.4, some applications of PS are discussed. The advantage of the tunable porosity and thickness of PS is exploited in fabricating Bragg filter structures (Paper II), which can be used as passive optical components in sensors. Anti-reflection coatings made on PS membranes are also demonstrated (Paper III). Because of the potential applications of PS and carbon nanotubes (CNTs) in field-effect devices (FEDs), oxidized PS membranes were used as growth templates for CNT synthesis by a catalytic chemical vapor deposition (CCVD) route (Paper VI). Finally, the high specific surface area and chemically-reductive feature of PS are exploited in the synthesis of Pd and Ag nanoparticles (Paper VII). Such catalyst systems can be implemented in the heterogeneous chemical catalysis.

Finally, the conclusions drawn in the thesis are presented in Chapter 5.

## **2 Synthesis and properties of porous silicon**

### **2.1 Fabrication of porous silicon by electrochemical etching**

In most cases, the porous silicon structure is formed by electrochemical etching of Si wafers in electrolytes including hydrofluoric acid (HF) and surfactants (mainly ethanol). Because the cleaned, polished Si wafer surface is hydrophobic, absolute alcohol is added to the electrolyte. It increases the wettability of the substrate and in turn helps the electrolyte penetrating into the pores, by which laterally homogenous current density can be maintained to result in the formation of uniform PS layers. During the electrochemical etching of a Si surface, H<sub>2</sub> gas evolves to form tiny bubbles attached to the surface. When ethanol is present in the electrolyte, these bubbles can easily leave the surface because of the decreased surface tension of the liquid. Additionally, the bubbling enhances the liquid circulation in the electrolyzation cell, which helps the transport of reactants and side products.

To be able to synthesize uniform layers with high reproducibility, the applied anodic current density and etching time are monitored, controlled and kept at a particular constant level required during the process. The electrolyzation cell is made of a highly-acidic resistant polymer such as polyvinylidene fluoride (PVDF) or polytetrafluoroethylene (PTFE). The cathode of the anodization cell is generally made of platinum or other HF-resistant conductive material, and the Si surface itself is the anode.

Based on the cell geometry, two main types of the anodization cells are distinguished in the literature of PS manufacturing (Halimaoui 1997). In Fig. 2, a conventional single-tank setup is shown. The backside of the Si wafer is placed on a metal disk and sealed with an O-ring on the frontside where the anodization takes place. Either high-dose impurity implantation of the wafers (e.g., boron for p-type and phosphorus for n-type) or an evaporated metal backside contact is necessary to provide an equipotential anodic contact, and to maintain uniform anodization current densities along the surface to be anodized. Because of the good homogeneity, easy porosity and thickness control, and enabled light exposure of the sample during the anodization process (which is necessary in the case of an n-type wafer), this kind of anodization setup is used most widely.

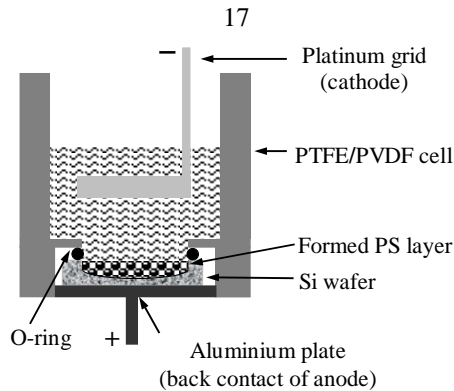


**Fig. 2. Schematic drawing of a conventional single-tank cell.**

Another popular type is the so-called double-tank anodization cell (Fig. 3). The two half-cells of the reactor are separated by a sealed Si wafer, and Pt plates are immersed symmetrically in both half-cells as electrodes. The electrolyte is circulated by a pump to remove the evolved gas bubbles from the Si surface and to keep the concentration constant in the bulk of the liquid. The power supply is connected to the Pt electrodes, and the current flows from one half to the other trough of the Si wafer. The backside of the Si wafer works as a secondary cathode, where the reduction of protons takes place and  $H_2$  evolves. The frontside of the wafer is the secondary anode, where the PS forms. Because the backside contact is electrochemical, no metallization is necessary to provide a uniform potential on the surface. In order to maintain reasonably-high current densities through the cell, highly-doped Si wafers are used.

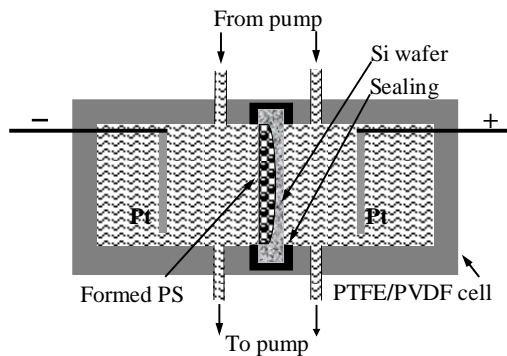


**Fig. 3. Cross-sectional view of a double-tank cell.**

The created samples are usually flushed in ethanol followed by drying. In this last step, cracking of the highly-porous or thick layers can be observed when the washing liquid evaporates from the pores. The origin of cracking is associated with the large capillary stresses arising in the nanometer size pores. To eliminate or reduce the problem, different drying processes have been investigated and introduced (Bellet 1997). The most efficient method is supercritical drying, using fluid  $CO_2$  at  $40^\circ C$  and pressures between

100-163 bar, for high-porosity samples. Another drying technique is so-called freeze drying, in which the specimens are impregnated with water or iso-butanol followed by freezing to  $-50\text{ }^{\circ}\text{C}$  and sublimation in vacuum. The third method applies the slow evaporation of water or ethanol used for rinsing. The fourth alternative is pentane drying: the samples are flushed in ethanol then dipped in pentane, which is evaporated from the pores.

The property of the formed porous silicon change during the storage, i.e., aging of the samples occurs. This phenomenon is correlated with chemical reactions proceeding on the surface of pore walls, and mainly concerns the oxidation of Si, which can take place in air and also in liquid media. Ultradry inert gas or ultrahigh vacuum storage can minimize the room temperature oxidation of freshly-etched samples. Ultrapure alcohol and highly-concentrated HF are suitable liquid storage media for a few hours or days. Basically, the storage conditions of a sample depend on the planned storage timescale and on the type of porous layer (Bellet 1997). Storage in the dark is generally recommended to minimize the oxidation associated with photochemical effects (Canham 1997).

## 2.2 Mechanism of silicon dissolution and pore formation

The structure of n- or p-type Si wafer is stable under cathodic polarization. The reduction of  $\text{H}^+$  to  $\text{H}_2$  is an only important reaction at the Si-electrolyte interface. However, the Si wafer dissolves under anodic polarization (Smith & Collins 1992, Bisi *et al.* 2000). Figure 4 shows the different regions of silicon dissolution as a function of the HF concentration in the electrolyte and the current density of the anodization process. To form a PS layer (under the solid line in the figure), one shall not exceed a certain current density limit at a given HF concentration; otherwise, the porous structure becomes inhomogeneous and some parts of it peel off from the substrate (between the dotted and solid lines). At high anodic potentials the Si wafer is electropolished (the region above the dotted line). When manufacturing freestanding PS membranes, the region of electropolishing plays a very important role. First, a porous layer is created on the wafer using a reasonably low current density, and then the current density is increased suddenly to a high value, i.e. to electropolish a thin layer of Si underneath the PS layer. This latter step results in the detachment of the PS membrane.

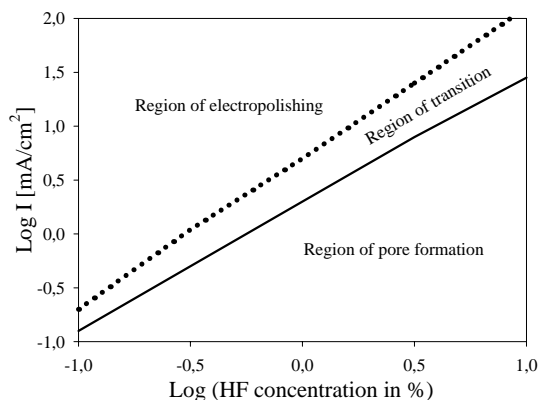


**Fig. 4. Regions of pore formation, transition and electropolishing of silicon at different HF concentrations (adopted from Smith & Collins 1992).**

Though the theory of the Si dissolution mechanism within the anodization process is not understood in all details yet, it is accepted that holes are required for both electropolishing and pore formation. In the case of an anodic polarization, the positively-charged Si surface is oxidized by  $F^-$  ions followed by the formation of water-soluble  $[SiF_6]^{2-}$  complex ions. For the pore formation, the anodic semireactions can be written as



In the case of electropolishing, the proposed reaction is



(Franssila 2004).

Lehmann and Gösele have proposed a Si dissolution mechanism in 1991, which is the most accepted theory. It is based on a surfacebound oxidization scheme, with hole capture and electron injection, and it leads to the Si oxidation state (Fig. 5).

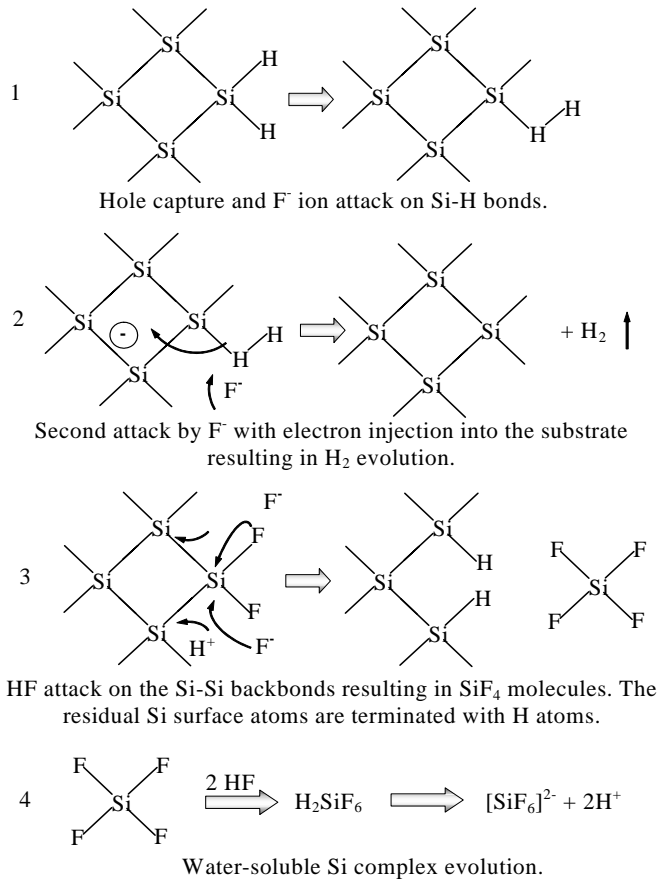


**Fig. 5. Anodic dissolution mechanism of Si according to Lehmann and Gösele (1991).**

The pore formation starts at a surface defect where the hole is available. Hence, the electrochemical dissolution of n-type Si requires the generation of hole-electron pairs e.g. by illumination (Goryachev *et al.* 2000, Kolasinski 2003).

In Fig. 6, the presumed band diagram of Si-PS and PS-electrolyte interfaces in equilibrium and during anodization are shown. When anodizing, two different ways are available for the hole to reach the surface (Lehmann *et al.* 1993). One way is straight to the bottom of the porous layer, and the other is through the Si wires of the skeleton to the surface of the pores (upper and right side in Fig. 6). In the first case, the holes flow without considerable resistance and can easily interact with the reactants on the solid-electrolyte interface. However in the second case, the holes need to pass through an ohmic interface between the Si bulk and the porous layer. Moreover, the holes passing through a network of Si wires represent only a very small current density on the surface of the pores, because of the high specific surface area of the skeleton. As a result, electrochemical etching is favored at the bottom of the porous structure.

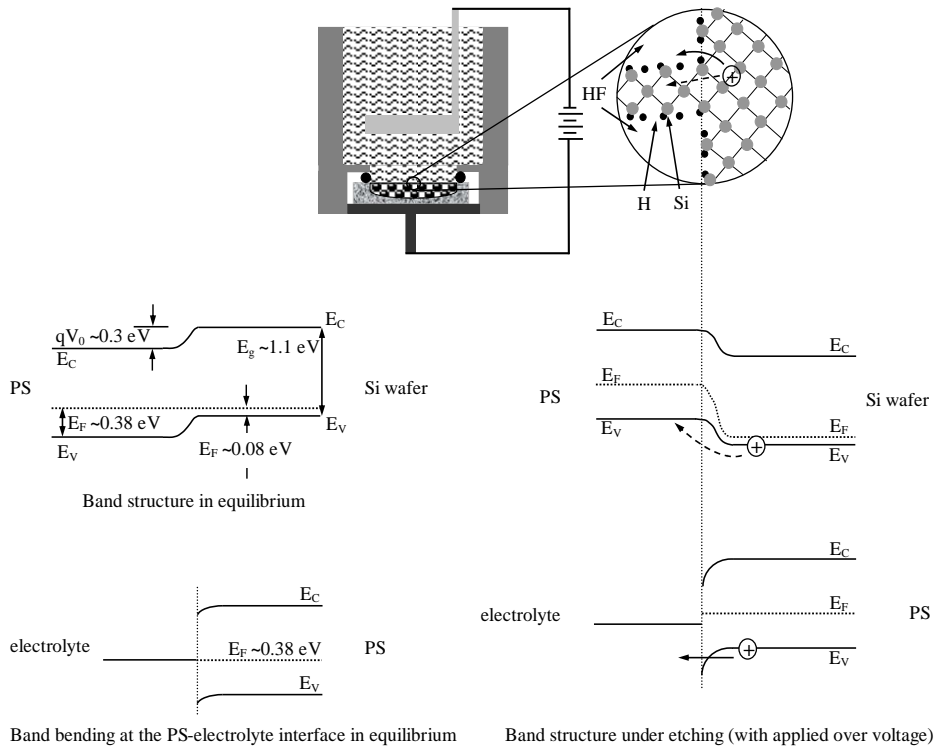


**Fig. 6. Band structure diagram of the PS-Si and PS-HF electrolyte interfaces (left side) in equilibrium (Mizsei *et al.* 2004 and Ottow 2005) and (right side) under the anodization process (modified and adopted from Lehmann *et al.* 1993).**

To determine the band diagram at the Si-PS and PS-electrolyte interfaces, some short calculations were carried out. The 0.08 eV value of the Fermi level in the bulk Si was obtained from the resistivity (0.015  $\Omega$ cm) of the  $p^+$ -type Si wafer. Using vibrating capacitor (Kelvin probe) and surface photovoltage (SPV) measurement techniques, Fermi level pinning at the Si-PS interface has been investigated on various PS layers formed on n,  $n^+$ , p and  $p^+$ -type Si by Mizsei *et al.* (2004). The contact potential at the  $p^+$ -Si-PS interface was found to be  $\sim 0.3$  eV, i.e., the Fermi level in the PS is  $\sim 0.38$  eV above the valence band. These data are shown in the equilibrium band structure sketch (upper and left sides in Fig. 6). In addition, the electrolyte-PS interface in equilibrium is shown (underneath and left side in Fig. 6), with a band bending at the interface (Ottow 2005). In our case, the band gap in the PS samples equals that of the original Si, where the gap widening for nanowires having diameter above  $\sim 10$  nm is not present (Read *et al.* 1992).

### 2.3 Key features of porous silicon layers

All physical parameters of PS, such as porosity, thickness, pore diameter and microstructure, depend on the composition of electrolyte, anodization current density, etching time, wafer type and resistivity, illumination (mainly in the case of n-type), temperature, ambient humidity and drying conditions (Table 1).

*Table 1. Effect of anodization conditions on the formation of porous silicon (taken from Bisi et al. 2000).*

Increasing the values of:	Porosity	Etching rate	Critical current
HF concentration	Decreases	Decreases	Increases
Current density	Increases	Increases	-
Anodization time	Slightly increases	Slightly decreases	-
Temperature	-	-	Increases
Wafer doping (p-type)	Decreases	Increases	Increases
Wafer doping (n-type)	Increases	Increases	-

Based on the porosity of PS, one can make a categorization using a macroscopic character of different porous layers, though it does not give any microscopic information such as pore size and shape. The porosity of samples ( $p$ ) is defined as the fraction of void in the porous structure,

$$p = \frac{m_1 - m_2}{m_1 - m_3}, \quad (3)$$

where  $m_1$ ,  $m_2$  and  $m_3$  denote the mass of the original, anodized and stripped wafer (in 1M NaOH solution), respectively. If the Si density is  $\rho$ , and  $A$  is the area of etched surface, the layer thickness ( $d$ ) is

$$d = \frac{m_1 - m_3}{\rho A}. \quad (4)$$

The porous structures are classified (IUPAC classification) by the average pore diameters such as micro, meso and macro-type, if the pore diameters are  $\leq 2$  nm, 2-50 nm and  $> 50$  nm, respectively. Originally, these properties and the spatial distribution of pores depend on the characteristics of the initial substrate and anodization conditions (Hérino 1997).

### 2.4 Chemical properties of porous silicon

The large specific surface area of PS (200 - 600 m<sup>2</sup>/cm<sup>3</sup>, Grosman & Ortega 1997) and chemical properties of the surface have an effect on the electrical, optical and mechanical properties. The pore surface includes a high density of dangling bonds of Si for original

impurities such as hydrogen and fluorine, which are residuals from the electrolyte. Additionally, if the manufactured PS layer is stored in ambient air for a few hours, the surface oxidizes spontaneously. Accordingly, the luminescent properties of PS layers related to hydrogen passivated dangling bonds show change (Yablonoitch *et al.* 1986). The surface oxidation causes a blue-shift in the luminescence spectra (Hossain *et al.* 2000, Karacali *et al.* 2003). In addition, the forming oxides alter the optical properties of the porous layer (Astrova *et al.* 1999), introduce mechanical stress (Paper IV) and also affect the electrical conductivity of the matter (Sailor 1997).

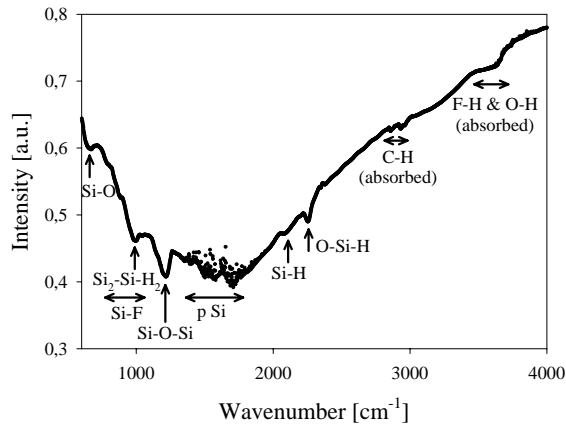


**Fig. 7. IR transmittance spectrum of a PS layer (Pap AE, unpublished data).**

The presence of original impurities is revealed by IR spectroscopy (Fig. 7). The hydrogen in the form of  $\text{SiH}_x$  ( $x = 1, 2, 3$ ) on the surface of a prepared PS layer can be observed. This original impurity remains on the surface after rinsing and drying the samples, but it desorbs during annealing at 300-500 °C (Vázsonyi *et al.* 1993). The freshly etched PS surface is saturated with hydrogen (Canham *et al.* 1991); therefore, the ratio of H/Si depends on the specific surface area. The original hydrogen passivation is stable for several months.

The fluorine is also an original impurity on the surface. Its concentration depends on the type of used electrolyte and is higher after etching in aqueous HF solution than that in ethanoic HF solution. The impurity is in the form of  $\text{SiF}_x$  ( $x = 1, 2, 3$ ). In contrast to hydrogen, the fluoride concentration decreases with time (Petit *et al.* 1997), probably because the SiF bonds are replaced by SiOH bonds through reactions with water vapor of air.

The anodization process alters the carrier distribution inside the Si skeleton, which causes a wide ‘peak’ in the spectrum (Timoshenko *et al.* 2001).

The freshly-prepared PS surface is oxidized in ambient air within an hour. The oxygen content is ~1-2 atomic %, which means that a small fraction of the surface is covered by  $\text{SiO}_2$  islands (Grosman & Ortega 1997). The Si/ $\text{SiO}_2$  ratio increases with time until the

whole surface is oxidized. Illumination and increased temperature enhance the oxidation reaction rate. The native oxide of an aged surface is not stoichiometric.

Impurities of carbon were also observed on the surface of PS by secondary ion mass spectroscopy (Hilliard *et al.* 1994). As revealed by Canham *et al.* in 1991, ethanol is not a source of such impurities, since carbon was also found on the surface after etching in ethanol free aqueous HF. Because the ratio of the oxygen and carbon is not correlated, the carbon impurity source is neither CO nor CO<sub>2</sub>. Hydrocarbons from the ambient air are thought to be the source of carbon impurities.

## 2.5 Physical properties of porous silicon

Barla *et al.* in 1984 showed that PS behaves similarly to the initial single crystal. However, due to the nanosize effects of lattice deformation, lattice mismatch occurs at the Si-PS interface. The Young's modulus for a PS layer decreases with increasing porosity and doping level (Bellet 1997). For instance, in the case of a p<sup>+</sup>-type Si wafer, the value of Young's modulus is 162 GPa, which reduces to ~0.87 GPa for a wafer of 90% porosity. The microhardness of the PS layer is also decreased with the porosity (Duttagupta *et al.* 1997).

The thermal conductivity of PS decreases with porosity; a nanoporous PS is a good thermal insulator. Though the published data in the literature show large scattering, the thermal conductivity of a macro- or mesoporous PS layer formed on a p<sup>+</sup> wafer can be estimated from the thermal conductivity of bulk material and the layer porosity. Additionally, in the case of nanoporous structures, the thermal conductivity is also dependent on the sample preparation process (Lang 1997).

Since PS is a spongy structure with an extremely-high specific surface area, the electrical resistivity of the layer is very high and is sensitive to the ambient atmosphere. Therefore, the determination of exact values for the PS resistivity is difficult (Ben-Chorin 1997). Amongst others, the resistivity depends on the quantum confinement, mobility and drift of the carriers, changes in the band structure and temperature, and on the medium (gas or liquid) filling the pores (Parkhutik 1999). The dielectric permittivity of PS decreases with increasing porosity in accordance with various EMAs (Ádám *et al.* 1995, Cox 1997).

The basic optical properties of a material are described by its complex refractive index. The wavelength-dependent effective refractive index of PS is affected by the porosity, the impurities bonded on the surface of pores and by the refractive index of the materials filling the pores. Experimentally the dispersion of refractive index is usually determined from optical reflection and transmission measurements utilizing the rules of optical interference and Fresnel's equations. It is also possible to perform measurements at a given wavelength, e.g., by a spectroscopic ellipsometer, and then run computer simulations to reveal spectral data for a system having multiple components (Fried *et al.* 1996). These methods are based on various EMAs (Bruggeman 1935, Looyenga 1965, Garnett 1904, etc.) in which the effective dielectric permittivities thus indirectly the effective refractive indices are correlated with the volume fractions and bulk permittivities of the components representing the mixture (Theiß & Hilbrich 1997). The

studies performed so far do not cover the whole spectrum, though the revealed refractive indices seem to follow the EMAs (Theiß 1997). The refractive index of an oxidized PS layer is lower than the non-oxidized form with the same porosity. The absorption coefficient of the PS layer shows correlation with the bandgap changes in the formed spongy structure and its porosity. The published data are based on optical transmission measurements, photoluminescence excitation (PLE) and photothermal deflection spectroscopy (PDS) techniques; and as concluded, the quantum confinement strongly affects the absorption of a PS material. In addition, widening of the bandgap and blue-shift of the absorption edge takes place (Bisi *et al.* 2000, Behren & Fauchet 1997).

A number of different luminescent phenomena occur in PS. Emission peaks were found around several center wavelengths from the UV to IR (Table 2). It is widely accepted that the origin of luminescent phenomena is the quantum confinement in the nanosize Si wires of the skeleton. Since the feature size of such light-emitting parts decreases with increasing porosity, the bandgap increases and causes shifts of the luminescence peaks in the spectra (Read *et al.* 1992).

*Table 2. Luminescence bands of porous silicon (adopted from Cullis et al. 1997 and Vinegoni et al. 2000).*

Spectral range	Peak wavelength	Label	PL	CL	EL
UV	~350 nm	UV band	yes	yes	no
Blue-green	~470 nm	F band	yes	yes	no
Blue-red	400-1100 nm	S band	yes	yes	yes
Near IR	1100-1500 nm	IR band	yes	no	no

Since the S band can be excited both phonically and electrically, it has certainly the most technological relevance. Due to the inhomogeneous broadening, the S band has large spectral width, where the position and intensity of the peak depend on the porosity. The photoluminescence (PL) efficiency is tunable; it is high under blue or UV, and low under red-yellow excitation. The model of the S-band photoluminescence is based on the quantum-confinement model (Cullis *et al.* 1997). The F band PL is strong in oxidized PS structures and is associated with the coexisting oxide (Vinegoni *et al.* 2000, Canham 1997). The near IR band peak position depends on the sample preparation process while its intensity is affected by the porosity and temperature. The model of the tunable IR band adopts the effects derived from the recombination model and the quantum-size effect theory (Sauer 1997). The UV band intensity increases with the oxide content of the PS sample. However, the position of the peak is well defined and is approximately at 350 nm (Qin & Lin 1997). Cathodoluminescence was observed during the structural study on PS and it is generated by the probe beam in the SEM and TEM devices. The peak of CL is extremely weak and unstable but it is stable and brighter when SiO<sub>2</sub> is present (Williams 1997). The third form of the luminescence is the electroluminescence, which is tunable by an electric field applied on the sample (Halimaoui *et al.* 1991). As a conclusion of the published results, the EL spectra show a large reversible blue shift with an increasing cathodic bias. Additionally, the PL spectrum is the envelope of all the emitted EL spectra observed on the same PS sample (Bsiesy 1997). Since the PL spectrum depends on the size of Si nanocrystallites in the PS skeleton, it suggests that the EL is also dependent on

the Si size. From the technological point of view, it is important to note that electrical contacts made on PS using Au, Ag, Al, Pt, ITO, etc. can be applied without influencing the EL phenomena (Cox 1997). Finally, chemiluminescence of PS was observed when the surface of PS was oxidized (Kooij & Kelly 1997).

## 2.6 Applications of porous silicon

Because of the designable materials properties, compatibility with conventional Si fabrication and thin film processes, and unique physical and chemical properties, PS is a versatile material with potential in a number of different application areas. Optical and optoelectronic applications are based on the tunable optical properties of the porous layer, such as the index of refraction and layer thickness (solar cells, PDs, reflectors), and on the various luminescence phenomena linked to PS (LEDs). The high specific surface area of the porous layer enables applications in chemical/biological sensing and can be exploited in future heterogeneous chemical catalysis. A new capacitor technology based on PS uses the advantage of the macroporous structures formed on n-type Si wafers (higher specific capacitance). In silicon micromechanics, PS is utilized as a sacrificial layer (in microlithography), active component (movable freestanding membrane, cantilever, etc.) or an insulator layer between conductive layers. The ELTRAN<sup>®</sup> (epitaxial layer transfer) method has been developed by Canon Incorporation (Japan) and it is based on the bond and etch-back of SOI, i.e., selective etching of PS and surface flattening are employed for micromechanics. Table 3 shows a compilation of relevant application areas based on the review paper of Parkhuitk (1999) and book chapters published in *Properties of porous silicon* (1997, edited by Canham) by Bondarenko & Yakovtseva, Thönissen *et al.*, Sailor, Canham, Lang, Menna & Tsuo, Lehmann and Yonehara, and other published papers by Rajamaran & Henderson (2005), Solanki *et al.* (2005), Bratkowski *et al.* (2005), Balucani *et al.* (2005), Volk *et al.* (2004), Yamazaki (2004), etc.

Table 3. Various applications of porous silicon.

Application area	Component based on PS	Utilized property of PS
Optical applications	Interference filter (Bragg, Fabry-Perot)	Tunable refractive index and layer thickness by manufacturing
	Solar cell (antireflection coating)	Tunable refractive index and layer thickness by manufacturing
	Waveguide	Tunable refractive index and thickness Direct integration with electrical components
Optoelectronic applications	Light emitting diode (LED)	Electroluminescence Schottky contact with some metals p-n junction without ion bombardment
	Photodetector (PD)	p-n junction without ion bombardment Wavelength dependent refractive index and absorption coefficient
	Field emission device (FED)	Free charge carriers generation
	Photonic crystal	Designable 2 and 3 D structure by periodically alternated layers with different refractive indices
Microelectronic applications	Optical logic gate	Nonlinear optical absorption
	Cold cathode	Electron and visible light emission from the surface at room/low temperature
	Epitaxial growth of silicon films on the PS surface	Suitable substrate for epitaxial growth
	Thermal / electrical insulation (IPOS, SOI, FIPOS)	Low thermal conductivity High electrical resistivity
Sensors and actuators	Silicon capacitor (SIKO)	Macroporous structure (n-type Si) High specific capacitance
	Micromechanical structures / MEMS	Selective etching of PS on Si
	Chemical sensors	Liquid or gas material sensing Electrical conductivity and capacitance effect Band structure change Photoluminescence quenching
Biological application	Sensing	Compatibility with the living organism Change of electrical and optical properties of PS by biomolecules

## 3 Experimental methods

### 3.1 Porous silicon synthesis and characterization

The PS samples, investigated in this thesis, were synthesized on p<sup>+</sup>-type Si wafers by anodic etching using a conventional single-tank electrolyzation cell (Fig. 2). The wafers were boron-doped (0.015 Ωcm) and polished along the (100) crystal plane direction. The electrolytes were prepared by mixing 50 wt% aqueous HF solution and absolute ethanol (C<sub>2</sub>H<sub>5</sub>OH) in various volumetric ratios. As listed in Table 1, the properties of the PS can be tuned through the manufacturing conditions, such as electrolyte concentration (*c*), current density (*J*) and etching time (*t*). The observed etching rates (*v*) of different processes and porosity (*p*) of the formed layers are collected in Table 4. The anodizing current densities were stabilized and the etching times were controlled by a computer. To create freestanding membranes an electropolishing step was applied in the last stage of anodization to detach the formed porous layers from the wafer. These current densities and time durations are also listed in Table 4. Each sample was flushed in absolute ethanol after synthesis and stored in pentane in a separate container. When it was applicable, the samples were freshly made before the particular post-fabrication and/or analyses processes.

The porosities of samples were calculated using Eq. (3). As described earlier, the mass of a skeleton could be calculated from gravimetric measurements after stripping the layer from the bulk in 1 M NaOH aqueous solution. Alternatively, the depth of the evolved groove in the Si bulk (which is eventually the same as the thickness of the PS layer) was measured by profilometry. Measurements of the layer thicknesses of freestanding membranes were carried out using microscopic techniques.

In Paper III, the repeatability and accuracy of sample preparation and characterization were investigated and reported. The results of error-calculations show that the relative standard deviation (RSD) of thickness measurements, by optical microscopy, is in the range  $1.5\% \leq \text{RSD} \leq 3.8\%$ . Due to the limited accuracy of mass measurements and repeatability of sample preparation, the relative standard deviation in the porosity is within the range  $0.5\% \leq \text{RSD} \leq 2.2\%$ .

Table 4. Etching rates and porosities of PS layers studied in different papers.

Electrolyte concentration	$J$ [mA/cm <sup>2</sup> ]	$v$ [nm/s]	$p$ [%]	Papers, where the samples were used
5 M HF and 15 M C <sub>2</sub> H <sub>5</sub> OH				
Sample 1	50	8.3	60	Paper VII
8.8 M HF and 12 M C <sub>2</sub> H <sub>5</sub> OH*				
Sample 2	20	14	70	Papers IV, V and VI
Sample 3	65	36	83	
11.7 M HF and 10.3 M C <sub>2</sub> H <sub>5</sub> OH**				
Sample 4	20	16	47	Papers I, II and III
Sample 5	35	36	52	
Sample 6	50	45	57	
Sample 7	65	55	61	
14.55 M HF and 8.5 M C <sub>2</sub> H <sub>5</sub> OH**				
Sample 8	20	27	41	Paper III

Electropolishing step applied after PS layer preparation: \*330 mA/cm<sup>2</sup>, 50 s, (except Paper VI), and \*\*500 mA/cm<sup>2</sup>, 10 s

The layer thickness of PS monolayer increases with the etching time and current density (Fig. 8), and the porosity is found to be independent of the anodization time.

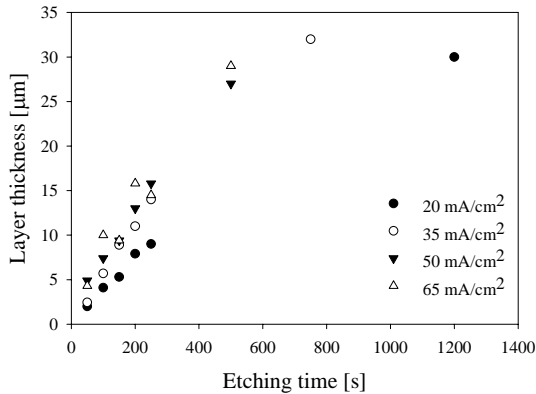
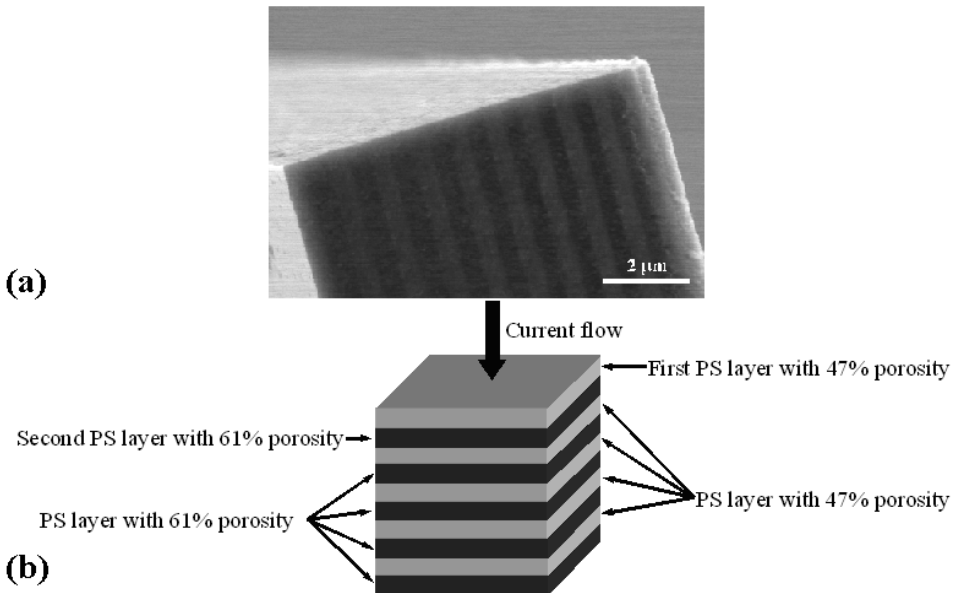


Fig. 8. PS layer thickness versus current density and anodisation time (in 11.7 M HF and 10.3 M C<sub>2</sub>H<sub>5</sub>OH).

Plan-parallel PS multilayer structures (10, 20, 30, 40 and 50 periods) were created by periodically alternating the anodization current densities and etching times ( $J_1 = 20$  mA/cm<sup>2</sup>,  $t_1 = 8$  s and  $J_2 = 65$  mA/cm<sup>2</sup>,  $t_2 = 4$  s) during the manufacturing process (Paper II). The multilayers were detached from the Si bulk with electropolishing to obtain freestanding Bragg gratings (Fig. 9).



**Fig. 9. (a) FESEM image of a freestanding, ten-periods PS multilayer. The dark and light zones have porosities of approximately 61% and 47%, respectively (Paper II). (b) Schematic draw of a five-periods PS multilayer.**

For both the low and high porosity layers, a slight variation in the thickness can be observed (Fig. 10). An explanation of the thickness variations is the reduced etching rate, which might be caused by diffusion-limited electrochemical reactions. Furthermore, the relatively quick switching between two different currents can cause transient effects in the process (e.g., polarization).

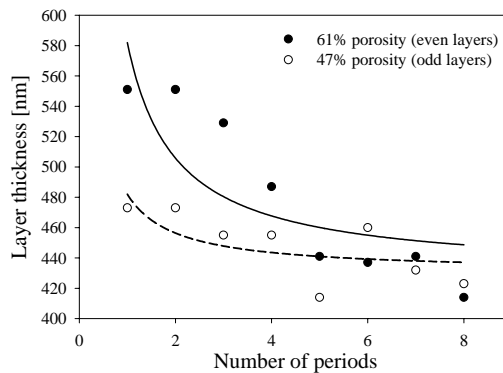


**Fig. 10. Layer thickness variation by the number of periods (Paper II).**

For the optical reflection measurements,  $\sim 200 \mu\text{m}$  - thick freestanding PS layers having different porosities were used (Paper III). Anti-reflection layers on the backsides of PS

samples were formed by increasing gradually the anodization current density at the end of the anodization process, in  $6.5 \text{ mA/cm}^2$  steps at every 2 s, until  $500 \text{ mA/cm}^2$  was reached.

### 3.2 Optical measurements

The wavelength-dependent refractive indices of PS monolayers of different porosities (Table 4) were calculated from optical transmission and reflection spectra. The spectra were recorded using an optical spectrum analyzer (Papers I, II and III). The experimental arrangements are sketched in Fig. 11.

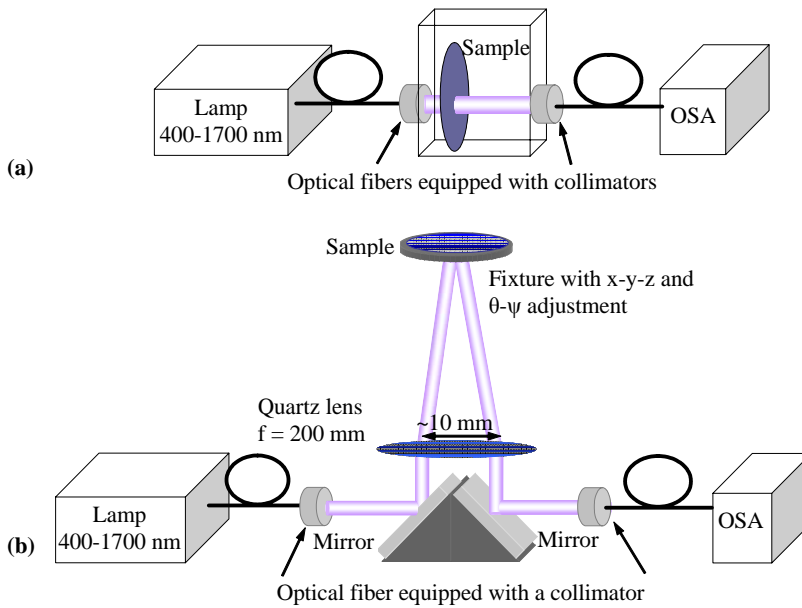


**Fig. 11. Schematics of the experimental setups used for (a) transmission and (b) reflection measurements. The transmitted beam is perpendicular to the sample, while in the reflection measurements the angle of the incidence is  $\sim 88.5^\circ$  (Paper III).**

The optical transmittance ( $T$ ) was calculated from the measured transmitted light intensities through the free optical ( $I_0$ ) path and the freestanding samples ( $I_S$ ), i.e.,  $T = I_S/I_0$ . PS monolayer membranes with different porosities of  $\sim 30 \mu\text{m}$  and  $\sim 15 \mu\text{m}$  thicknesses were investigated in Papers I and III, respectively. In Paper II, the same setup was used for recording the transmittance spectra of the freestanding Bragg filters having 20, 40, 60, 80 and 100 layers.

In the case of reflection measurements, the reference intensity ( $I_{M(0)}$ ) was set up using a gold mirror at the position of the sample. The reflected intensity from the mirror ( $I_M$ ) was measured, and then corrected for the wavelength-dependent reflectivity of the mirror ( $f_C$ ) (Edmund catalog, 2004), as  $I_{M(0)} = I_M/f_C$ . Thus, the reflectivity of the samples ( $R$ ) is

obtained as  $R = I_S/I_{M(0)}$ , where  $I_S$  denotes the reflected light intensity from the PS surface. The intensity of the reflected light from the mirror and from the thick ( $\sim 200 \mu\text{m}$ ) freestanding PS membranes was recorded. Each sample was prepared with an anti-reflection layer on the backside (Paper III).

In Papers I and II, the measured wavelength range was 400 -1700 nm. In Paper III, the previously published transmission measurements performed on single PS membranes (in Paper I) were repeated with higher accuracy, in the range 700-1700 nm with a 0.2 nm step size and average of twenty measurements for each wavelength.

### 3.3 Dry thermal oxidation

Freestanding PS membranes with  $\sim 30 \mu\text{m}$  thickness and  $\sim 70\%$  and  $\sim 83\%$  porosities were used in the experiments (Table 4). The thermal oxidation of the samples was carried out in air at 473, 673, 873 and 1073 K for 1, 2, 5, 10 and 20 h time durations (Papers IV and V) using a box-furnace (Logotherm N7). Low heating and cooling rates (5 K/min) were applied to minimize the stress in the samples. The oxidation extents in the samples were calculated from gravimetric measurements (accuracy  $\sim 2\%$ ).

### 3.4 Carbon nanotube synthesis

PS layers with  $\sim 70\%$  porosity and  $\sim 30 \mu\text{m}$  thickness on Si support were used as starting materials (Table 4). The samples were oxidized in dry air at 473, 673, 873 and 1073 K oven 1 h. Finally, multi-wall carbon nanotubes (MWCNTs) were grown on the samples by CCVD using a mixture of xylene and ferrocene. The growth was carried out at 1043 K in argon flow (with  $30 \text{ cm}^3/\text{min}$  flux at 1 atm pressure). The solution of 10 g ferrocene in  $1000 \text{ cm}^3$  xylene was fed at a rate of  $0.1 \text{ cm}^3/\text{min}$  into an evaporator column preheated to 458 K, from which the vapor of ferrocene and xylene was introduced into the tube reactor. Deposition times of 20 and 90 minutes were applied (Paper VI).

### 3.5 Simultaneous chemical silver and palladium deposition

PS layers of  $\sim 60\%$  porosity and  $\sim 5 \mu\text{m}$  thickness on Si wafer were applied (Table 4). The metallization was executed in various mixtures of 0.05 M  $\text{Pd}(\text{ac})_2$  and 0.05 M  $\text{AgNO}_3$ , 2 M  $\text{NH}_4\text{OH}$  electrolytes. After metal deposition, the samples were rinsed in distilled water and dried with pressurized  $\text{N}_2$ .

When the dependence of the deposition on the metal ion concentrations was examined, the ratio of  $[\text{Pd}(\text{NH}_3)_4]^{2+}$  and  $[\text{Ag}(\text{NH}_3)_2]^+$  complex ions were 1:0, 9:1, 4:1, 2:1, 1:1, 1:2, 1:4, 1:9 and 0:1. The plating time was 10 s. In the course of the rest of the experiments, this ratio was constant 4:1, while plating times of 10, 30, 60 and 120 s were applied. Some of the samples were annealed in a belt furnace at 523, 723 and 1023 K for 15 min, with 7.5 min heating and 7.5 min cooling profiles, in normal atmosphere.

### 3.6 Analyses and measurements

The profiles of grooves formed on Si wafers after stripping off the PS layers were measured by a Dektak<sup>3</sup> ST surface profilometer. Direct thicknesses measurements and optical investigations of various samples were accomplished using an Olympus BH-2 optical microscope equipped with a digital camera system. Surface imaging and elemental analyses of the samples were carried out using scanning electron microscopy (SEM, Jeol JSM-6400) and field emission scanning electron microscopy (FESEM, Jeol JSM-6300F), both equipped with energy dispersive X-ray analysis (EDX) devices. High resolution imaging and elemental analyses of nanostructures were performed using energy-filtered transmission electron microscopy (EFTEM/EDX, Leo 912 Omega). Surface morphologies were studied with an atomic force microscope (AFM, NanoScope II scanning tunneling microscope). The crystal structures of different specimens were analyzed by X-ray diffraction (XRD, Philips X-ray equipment and Siemens D5000). Optical spectra were recorded with an optical spectrum analyzer (ANDO AQ-6315). IR spectra were recorded using Fourier-transmission infrared spectroscopy (FTIR, Bruker FRA 106).

## 4 Results and discussion

### 4.1 Optical properties of porous silicon

#### 4.1.1 Study on layers of uniform porosities

The envelope method, described by Manifacier *et al.* in 1976, enables us to calculate the refractive index, absorption coefficient and layer thickness of a thin, weakly-absorbing dielectric film from the measured transmission spectrum in a non-absorbing surrounding medium. Applying this theory to our PS membranes, the wavelength-dependent refractive indices of thin freestanding PS layers were determined by

$$n_{\text{PS}}^{\text{env}} = \sqrt{N + \sqrt{N^2 - n_0^2 n_1^2}} \quad (5)$$

$$N = \frac{n_0^2 n_1^2}{2} + 2n_0 n_1 \frac{T_{\text{max}} - T_{\text{min}}}{T_{\text{max}} T_{\text{min}}}, \quad (6)$$

where  $T_{\text{max}}$  and  $T_{\text{min}}$  are the envelope functions of the local minima and maxima of oscillations in the transmission spectrum, and  $n_0$  and  $n_1$  are the refractive indices of the media in front and behind the film. In our case  $n_0 = n_1 = 1$ , because the optical transmission measurements were accomplished in air (Papers I and III).

According to the theories of various EMAs – from an optical point of view - a mixture of different materials can be considered as a homogenous medium having an effective index of refraction which is obtained from the refractive indices and the volume fractions of components. Applying Bruggemans's EMA (Arrand HF, 1997),

$$n_{\text{PS}}^{\text{EMA}} = \frac{1}{2} \sqrt{3p(1 - n_{\text{Si}}^2) + (2n_{\text{Si}}^2 - 1) + \sqrt{(3p(1 - n_{\text{Si}}^2) + (2n_{\text{Si}}^2 - 1))^2 + 8n_{\text{Si}}^2}}, \quad (7)$$

the effective index of refraction for a PS layer,  $n_{\text{PS}}^{\text{EMA}}$ , having porosity  $p$ , can be derived from the refractive index of Si,  $n_{\text{Si}}$ . It is a prerequisite in the EMAs that the wavelength of electromagnetic radiation is larger than the size of various features in the mixture.

The measurement and computation of wavelength-dependent refractive indices for layers of different porosities were accomplished using the envelope method and Bruggeman's EMA. The calculated refractive indices (at  $800 \text{ nm} < \lambda$  using Eqs. (5) and (6)) of the PS samples were in qualitative agreement with those expected by the EMA (Eq. (7)), i.e., a higher porosity results in a lower index of refraction and *vice versa*. However, the experimental refractive indices, calculated with the envelope method, were lower than those calculated with the Bruggeman's theory. Furthermore, unexpected anomalous dispersion of the index of refraction was also observed. Concerning the optical absorption the transmitted light intensity increases with porosity, and the membranes have poor transparency at shorter wavelengths ( $\lambda < 800 \text{ nm}$ ) because of the fundamental optical absorption in Si (Paper I).

In order to reveal the origin of the anomalous optical dispersion presented in Paper I, the transmission measurements were improved and repeated with higher accuracy (Paper III). The results of these experiments and calculations suggest that the source of the anomaly is in the envelope method itself. The refractive index values, given by the envelope method, depend on  $T_{\text{max}}$  and  $T_{\text{min}}$ . Since the measured refractive indices are lower than those expected from EMA, the envelope functions are not opened up, i.e. the local  $T_{\text{max}}$  is lower and the local  $T_{\text{min}}$  is higher compared to the real case. Physically, this can be attributed to optical losses such as light absorption and scattering, when measuring the transmittance of the thin films. Although the envelope method includes the parameter of absorption for weakly absorbing media, the only plausible explanation for the supposed losses is optical scattering in the measured porous samples. Furthermore, the observed anomaly in the refractive indices suggests that light scattering is lower in the IR than the visible range.

To verify this presumption, besides the measured transmission spectra, optical reflection spectra of  $\sim 200 \mu\text{m}$  - thick freestanding PS samples with anti-reflection layer on their back-sides were recorded (Paper III). The porosities of the samples were the same as those in the transmission measurements. The reflection of the polished p<sup>+</sup>-type Si wafer has also been recorded, and the wavelength-dependent refractive index of the Si has been calculated using the Fresnel's equation for an air-Si interface

$$R_{\text{Si}} = \frac{(n_{\text{Si}}^{\text{Fresnel}} - 1)^2}{(n_{\text{Si}}^{\text{Fresnel}} + 1)^2}, \quad (8)$$

where  $R_{\text{Si}}$  denotes the recorded dispersion curve of the Si wafer. From Eq. (8), the wavelength-dependent refractive index of Si  $n_{\text{Si}}^{\text{Fresnel}}$  was calculated and used in the EMA computations (Eq. (7)) to yield the effective index of refraction  $n_{\text{PS}}^{\text{EMA}}$  for the PS layers.

In the next stage of the study, the theoretical reflectances of the PS membranes were determined by inserting the corresponding  $n_{\text{PS}}^{\text{EMA}}$  data in Fresnel's formula. In addition, from the recorded  $R_{\text{PS}}$  reflection spectra of various PS samples, new sets of experimental refractive indices  $n_{\text{PS}}^{\text{Fresnel}}$  were also obtained from Fresnel's equation.

The experimentally-determined  $n_{\text{PS}}^{\text{Fresnel}}$  data values are also lower than the corresponding theoretical ones  $n_{\text{PS}}^{\text{EMA}}$ . At shorter wavelengths ( $\lambda < 1000$  nm), the measured reflectivities are significantly lower than the theoretical, though the differences tend to decrease for longer wavelengths ( $1000 \text{ nm} < \lambda$ ).

These observations also support the presence of optical scattering. Considering a typical feature size of  $d \sim 30$  nm for the average pore diameters and Si wall thickness in the skeleton, the size parameter

$$a = \frac{\pi d}{\lambda} \quad (9)$$

is approximately between 0.13 and 0.06 for the applied wavelength range. This satisfies the criterion for Rayleigh scattering, where the scattered intensity is proportional to  $a^4$ . It means that the scattered intensity is about thirty times smaller at 1700 nm than that for 700 nm, which seems to be in agreement with the phenomena observed in the reflection spectra of various PS films.

In order to visualize the scattering on the porous surface, a PS sample and a pristine Si bulk were illuminated using a visible HeNe laser beam (633 nm, TEM<sub>00</sub>). In the case of the PS surface, the spot of the incident laser beam can clearly be seen from any direction indicating that light is scattered over the whole solid angle (Fig. 12 (a)) according to the isotropic nature of Rayleigh scattering. On the contrary, the surface of a pristine Si wafer behaves as a secularly-reflecting mirror: the spot of the incident laser beam is practically invisible from any direction different than the optical axes (Fig. 12 (b)).

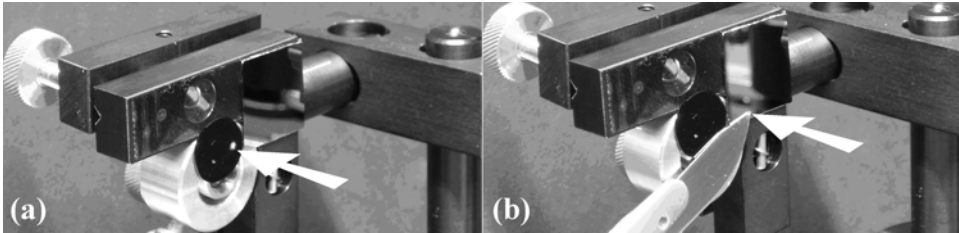


**Fig. 12. Demonstration of light scattering from the surface of a PS layer (a) and from the surface of a p<sup>+</sup> pristine wafer (b). The incident beams are shown with the white arrows (Paper III).**

The reflection measurements demonstrated the presence of light scattering on the PS surface, but did not solve the computation problem of the refractive indices. The envelope method and the calculation from Fresnel's equation, used to recover the refractive indices failed to provide accurate data. Both methods are unable to handle the intensity loss caused by scattering. However, one can overcome such limitation using the relationship between the layer thickness ( $t$ ), refractive index and positions of the extrema,

$$n_{\text{PS}}^{\text{int}} = \frac{M\lambda_1\lambda_2}{2t(\lambda_2 - \lambda_1)}, \quad (10)$$

where  $M$  is the number of oscillations (fringes) between the two extrema at  $\lambda_1$  and  $\lambda_2$ .

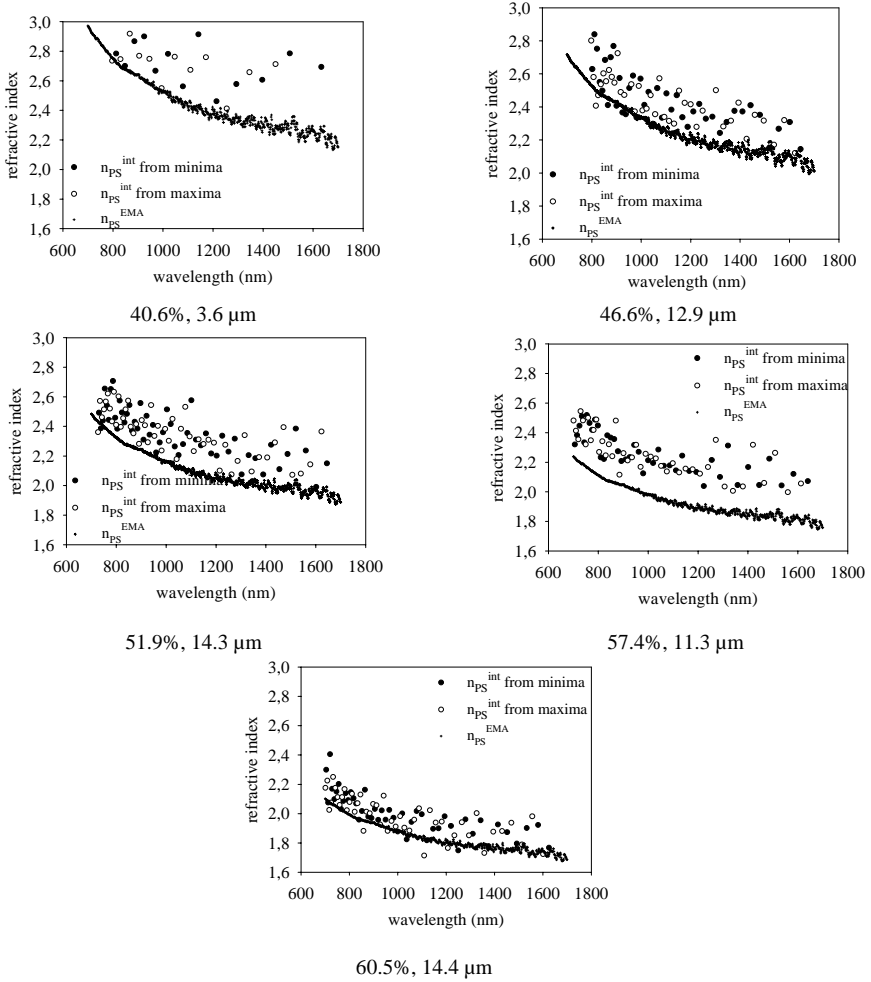


**Fig. 13. Refractive indices of PS layers as calculated from the position of the extrema in the optical transmission spectra and from Bruggeman's EMA, using the experimentally-determined wavelength-dependent refractive index of the p<sup>+</sup>-type Si (Paper III).**

The equation can be used for thickness determination if the refractive index is known, or *vice versa*, for calculating the refractive index if the layer thickness is known (e.g. from direct microscopy measurements). Applying the latter case, from the positions of local minima and maxima in the transmission spectra, the  $n_{\text{PS}}^{\text{int}}$  data for various PS films were

determined. The extracted results show good matching with those obtained previously from EMA (Fig. 13). In addition, Paper III gives more new scientific information about the refractive indices of PS (in the visible and near-IR range) and the effect of optical scattering at the air-PS surface on the transmitted or reflected light intensity.

Using the accurate refractive indices, one can approximate the corresponding values of the  $T_{\max}$  and  $T_{\min}$  envelopes for the idealized transmission spectra by applying Eqs. (5) and (6). By substituting the measured PS layer thickness, the accurate index of refraction and the approximated  $T_{\max}$  and  $T_{\min}$  values into

$$\alpha = -\frac{1}{t} \ln \frac{(n_{\text{PS}} + n_0)(n_1 + n_{\text{PS}}) \left(1 - \sqrt{T_{\max}/T_{\min}}\right)}{(n_{\text{PS}} - n_0)(n_1 - n_{\text{PS}}) \left(1 + \sqrt{T_{\max}/T_{\min}}\right)}, \quad (11)$$

one gets the approximated absorption coefficients for the PS film. These values are typically similar or slightly smaller than those obtained directly from the envelope method (Papers I and III).

#### 4.1.2 Investigation of layers with alternating porosities

The optical transmission of plane-parallel multilayer PS structures was investigated. In the samples, low ( $n_L$ ) and high ( $n_H$ ) refractive index layers having certain thickness ( $t_L$  and  $t_H$ ) were alternated periodically (Paper II). The centre of the wavelengths where strong reflection occurs is given by the Bragg condition (Snow *et al.* 1999),

$$\lambda_{\text{Bragg}} = \frac{2}{m} (n_L t_L + n_H t_H), \quad (12)$$

where  $m$  is the order (an integer). The spectral width of the reflection band depends on the center wavelength and on the number of layers  $N$  in the stack (Fraçon 1966):

$$\delta\lambda_{\text{Bragg}} = \frac{2\lambda_{\text{Bragg}}}{N}. \quad (13)$$

As can be seen from Eqs. (12) and (13), any variations in the thickness (Fig. 11) or in the refractive index (Fig. 14) of layers result in a shift of the reflection:

$$\Delta\lambda_{\text{Bragg}} = \frac{2(n_L \Delta t_L + t_L \Delta n_L + n_H \Delta t_H + \Delta n_H t_H)}{m}. \quad (14)$$

Due to the spectral broadening of each reflected wavelength ( $\delta\lambda_{\text{Bragg}}$ ), which is usually in the range of a few tens of nanometers, the multilayer structures reflect within wavelength intervals rather than at certain wavelengths.

The reflected light intensity depends on the refractive indices and numbers of layers in the stack. If absorption is neglected, the reflectance ( $R$ ) of such a multilayer structure (with  $N + 1$  layer) at normal incidence is

$$R = \left( \frac{n_0 - (n_H/n_L)^N n_H^2/n_0}{n_0 + (n_H/n_L)^N n_H^2/n_0} \right)^2, \quad (15)$$

where  $n_0$  is the refractive index of the ambient medium (Hawkes & Latimer 1995). The optical absorption can be neglected in  $R$ , because at  $800 \text{ nm} < \lambda$  the absorption of the PS is very low. However, optical scattering is also present at the air-PS surface, so that the reflected light intensity is lower than in the ideal case.

As described in Chapter 3.1, Bragg gratings with 20, 40, 60, 80 and 100 alternating layers were fabricated, and the optical transmission spectra of the filters were measured (using the setup of Fig. 11 (a)). Close to the visible wavelengths, the transparency is low due to the fundamental optical absorption of Si. As the number of periods is increased, a wide non-transparent band appears above 1500 nm (Fig. 14 (b)) and shifts gradually towards the shorter wavelengths down to 1080 nm (Fig. 14 (e)). Using the typical layer thickness values (Fig. (9)) of  $t_H \sim 440 \text{ nm}$  and  $t_L \sim 450 \text{ nm}$  for the layers having  $n_H$  and  $n_L$  index of refraction (Paper III), the Bragg orders  $m$  for the stop bands in the measured 400-1700 nm spectrum ranges were calculated. The observed stop band, at the longer wavelengths, is the 2<sup>nd</sup> harmonic of the first Bragg condition. The band appearing around 900 nm corresponds to the merged bands of the 4<sup>th</sup> and 5<sup>th</sup> Bragg condition, and the 3<sup>rd</sup> harmonics is most likely merged with the 2<sup>nd</sup> one. Finally, the shift and broadening of reflection bands are due to the thickness variation in the layers and the normal dispersion of refractive indices.

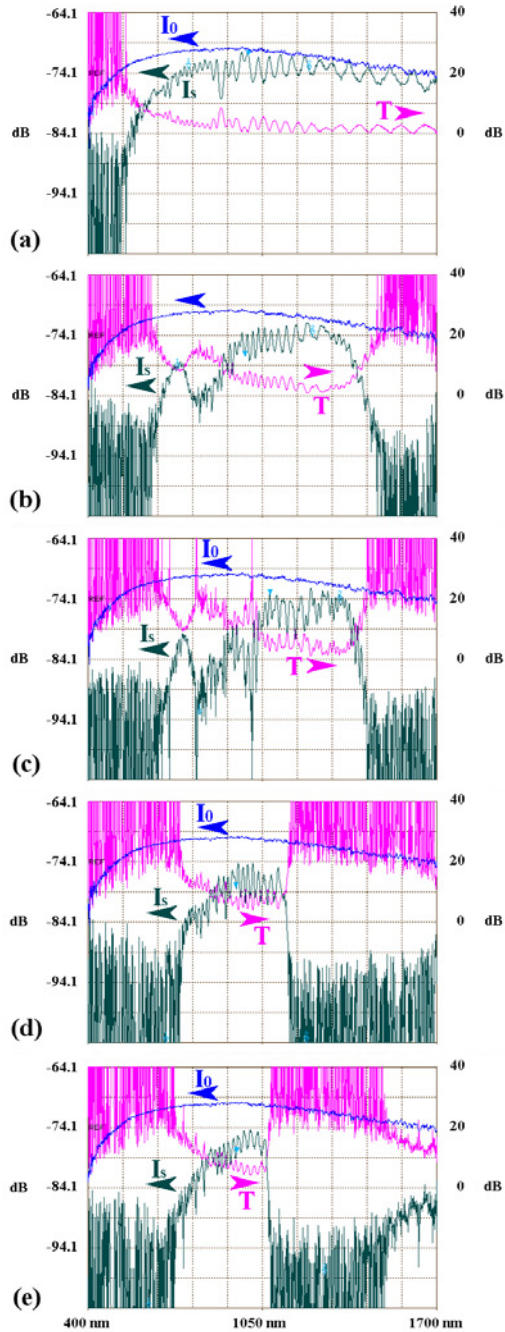
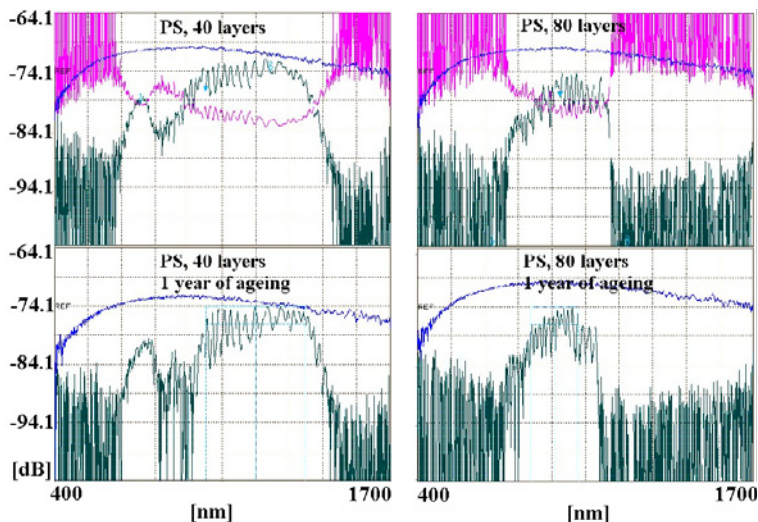


Fig. 14. Optical transmission spectra of (a) 20, (b) 40, (c) 60, (d) 80 and (e) 100 alternating PS layers (Paper II). The optical transmissions of samples (T) are calculated from transmitted intensities without ( $I_0$ ) and with ( $I_s$ ) the PS multilayer. The manufacturing parameters are described in Chapter 3.1.

As presented in Chapter 2.4, PS might undergo spontaneous oxidation, i.e. the Si skeleton partly turns into  $\text{SiO}_2$ , when the samples are stored in ambient air. The optical transmission spectra of two Bragg filters were re-measured after a year of storage (Fig. 15). The changes in the spectra are not significant, although a slight blue-shift and the reduction of transmittance in both re-measured spectra can be observed.



**Fig. 15. Repeated transmission measurements carried out on Bragg filters after one year from the sample preparation (Pap AE, unpublished data).**

These changes in the optical transmission spectra indicate the appearance of impurities, which decrease the effective refractive indices of the layers (blue-shift) and increase the absorption and/or the scattering in the layers.

## 4.2 Dry thermal oxidation of porous silicon

### 4.2.1 Study on structure

Oxidation of PS can result in changes in the porous structure. To investigate the effects of oxidation on the structure of PS, various samples were prepared and oxidized as described in Chapter 3. The investigations were carried out using FESEM, AFM, EFTEM/EDX, XRD and gravimetric measurements (Paper IV).

During oxidation, a certain fraction of Si skeleton turns into  $\text{SiO}_2$ . The degree of oxidation  $ox$  is defined by the ratio of oxygen built in  $n_{\text{O}_2}$  and the initial silicon amount  $n_{\text{Si}}$ . These were measured via the mass gain ( $m_1 - m_0$ ) as

$$ox = \frac{n_{\text{SiO}_2}}{n_{\text{Si}}} = \frac{n_{\text{O}_2}}{n_{\text{Si},0}} = \frac{m_t - m_0}{m_0} \frac{M_{\text{Si}}}{M_{\text{O}_2}}, \quad (16)$$

where  $M_{\text{O}_2}$  and  $M_{\text{Si}}$  are the molar masses of the oxygen and silicon, respectively (Paper V). Since the initial amount of Si changes considerably during the heating/cooling steps (the  $ox \neq 0$  values at  $t = 0$  show the extent of oxygen taken up within the heating and cooling ramps), reference samples were made and the measurement data were corrected to eliminate the amount of  $\text{SiO}_2$  formed in the transients (i.e., at  $t = 0$  there is no  $\text{SiO}_2$  in the structure) as

$$ox^* = \frac{n_{\text{O}_2}^*}{n_{\text{Si},0}^*} = \frac{n_{\text{O}_2} - ox_0 \cdot n_{\text{Si},0}}{(1 - ox_0) \cdot n_{\text{Si},0}}. \quad (17)$$

Analyses using FESEM could not reveal any considerable difference between the original and oxidized porous structures. Therefore, the volumetric gain of the skeleton and the change in pore sizes were calculated from Eq. (18), using the molar density of Si and  $\text{SiO}_2$ . Considering an average pore diameter of  $\sim 30$  nm in the non-oxidized PS layers (Fig. 16), after oxidation it decreases to 23-29 nm due to the lower molar density of  $\text{SiO}_2$ . The resulting  $\text{SiO}_2$  volume was calculated using

$$V_{\text{SiO}_2} = \frac{V_{\text{Si}} \rho_{\text{Si}} M_{\text{SiO}_2}}{\rho_{\text{SiO}_2} M_{\text{Si}}}, \quad (18)$$

where  $\rho_{\text{Si}}$  and  $\rho_{\text{SiO}_2}$  are the densities of the Si and the  $\text{SiO}_2$ , respectively, and the  $V_{\text{Si}}$  is the volume of the initial Si.

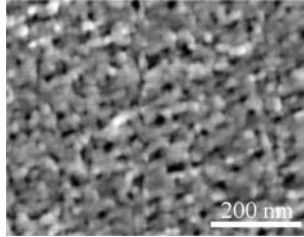


**Fig. 16. FESEM picture of a pristine PS layer (porosity is  $\sim 70\%$ ). The structure consists of 10-40 nm diameter holes confined with Si walls having a mean size of  $\sim 30$  nm (Paper IV).**

Consistently, the porosity of oxidized samples  $p_{ox}$  can be calculated from the original porosity of the PS membrane  $p$  and the extent (or degree) of oxidation  $ox$ :

$$(1 - p_{ox}) = (1 - p)(1.6ox + 1). \quad (19)$$

The surface morphology of the oxidized PS layers was investigated using AFM and compared to non-oxidized PS (Fig. 17). Changes in the roughness and the height of the surfaces mean were revealed. The evolution of gentle spherical surface features of the fully-oxidized samples could be seen. The rounded shapes on the surface indicate that the formed  $\text{SiO}_2$  is amorphous.

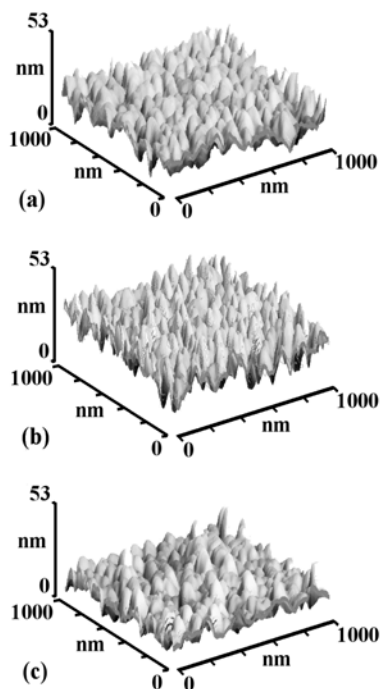


**Fig. 17.** AFM morphology of the sample (a) non-oxidized, (b) oxidized at 673 K, and (c) oxidized at 1073 K for 10 h (Paper IV).

The TEM analysis verified the presence of  $\text{SiO}_2$  in amorphous form. As was observed, the well-defined step crystalline edges become diffuse, indicating that the Si skeleton turns into an amorphous form (Fig. 18).

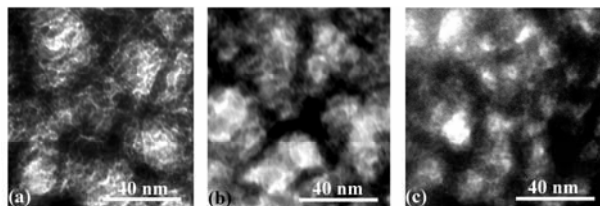


**Fig. 18.** At a higher oxidation temperature, Si is increasingly transformed to  $\text{SiO}_2$ , with consequential loss of crystalline structure, resulting in a partly-amorphous form. Images are made by TEM for non-oxidized (a), at 473 K (b) and 873 K (c) during 1 h oxidations (Paper IV).

To investigate the effect of oxidation on the properties of the crystal structure of the samples, X-ray diffraction analyses were carried out in the  $13^{\circ}$ - $80^{\circ}$  range of  $2\Theta$ . It was found that the intensity of Si(400) reflections decreases and the position of the peaks shifts towards the lower  $2\Theta$  angles (Fig. 19). The decreased peak intensities imply the consumption of crystalline Si in the skeleton. Since no other reflections are found at the applied angle range, the formed  $\text{SiO}_2$  phase proved to be amorphous. The shift of the Si(400) peak can be explained by stresses evolving in the crystal lattice during oxidation. The non-uniform strain distribution in the porous structure and the decrease of the Si size causes a broadening of the Si(400) peaks.

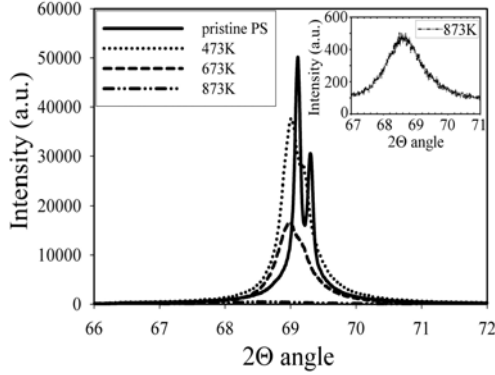


**Fig. 19. XRD curves of oxidized samples, created at different temperatures and 10 h duration (Paper IV).**

The exact position of the shifted Si(400) X-ray diffraction peaks was determined by fitting doublets of Lorentzian peaks. From Bragg's law,  $2d \sin \Theta = \lambda$ , the relative lattice deformation can be derived as

$$-\frac{\Delta d}{d_0} = \frac{\Delta \Theta}{\text{tg} \Theta}, \quad (20)$$

where the symbol  $\Theta$  denotes the corresponding half angle of the shifted Si(400) peaks,  $d$  is the new lattice spacing in the residual Si skeleton,  $d_0$  is the lattice spacing in the non-oxidized PS, and  $\lambda$  is the wavelength of the  $\text{Cu } K\alpha_1$  radiation. The position of the observed Si(400) peak in the pristine PS layer was  $2\Theta = 69.148^{\circ}$  within the accuracy of the measurement. Plotting the calculated strain data (Fig. 20), the deformation increase is found up to 873 K for both 1 and 10 h oxidation periods. At 1073 K and 1 h, the relative lattice deformation turns back significantly.

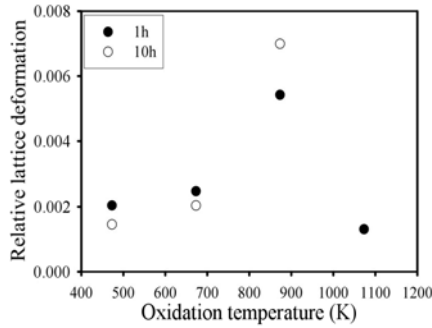


**Fig. 20. Relative lattice deformation of oxidized PS structures having various oxidation extents versus the oxidation temperature and duration (Paper IV).**

At 1073 K and 1 h, the amount of the residual Si is ~20%, and due to the formed stress, the Si skeleton breaks and lattice relaxes. This means that the lattice deformation is induced by a thermal expansion coefficient mismatch between the grown SiO<sub>2</sub> and the residual Si. During the heating and cooling periods, positive and negative strains evolve, respectively. Because the difference is significant in the thermal expansion coefficients, the formed oxide inhibits the relaxation of the PS skeleton. The stresses in the structure can be relaxed when the amount of the residual Si is low enough. Moreover, besides the thermal stress, a large intrinsic stress accumulates at the Si-SiO<sub>2</sub> interface because of the difference in the distances between the Si-Si and Si-O bonds (Tóth *et al.* 2005). These explanations of the relative lattice deformations are supported by three-dimensional thermomechanical modeling using the finite-element method (FEM). In Table 5, the simulated strain is compared to the measured ones and show good matching.

*Table 5. Measured and simulated strain in oxidized PS layers (Paper IV).*

Oxidation extent	Simulated strain		Total simulated strain	Measured strain
	Thermal	Intrinsic		
~10% (473K/1h)	$2.08 \times 10^{-5}$	$1.67 \times 10^{-3}$	$1.69 \times 10^{-3}$	$2.0 \times 10^{-3}$
~50% (873K/1h)	$2.75 \times 10^{-4}$	$1.98 \times 10^{-3}$	$2.26 \times 10^{-3}$	$5.4 \times 10^{-3}$

#### 4.2.2 Study on reaction kinetics

The aim was to examine how the thermal oxidation of PS proceeds and to reveal the peculiarities of chemical reaction kinetics (Paper V). The oxidation extent of PS samples was calculated from Eqs. (16) and (17). Plotting the calculated results as a function of oxidation temperature and time, a saturation curve can be observed (Fig. 21). At 473 and 673 K the curves saturate to 0.16 and 0.33, respectively. At higher temperatures, the oxidation is faster, and the achieved SiO<sub>2</sub> concentrations are much higher compared to the corresponding lower temperature measurements. At 1073 K, the oxidation saturates to 1, i.e., the entire amount of PS turns into porous SiO<sub>2</sub> within 10 hours. Though the curve for

873 K shows a monotonic increase with time, saturation could not be observed due to the short time frame.

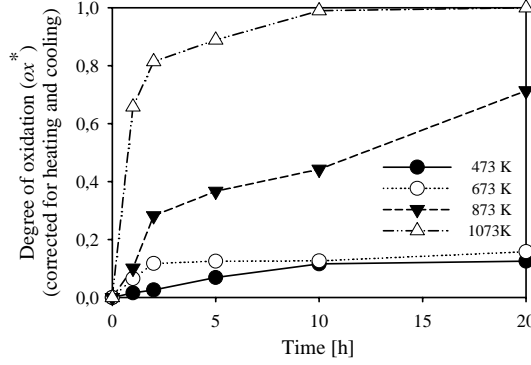


**Fig. 21. Oxidation extent of 70% porosity and 30  $\mu\text{m}$  - thick PS membranes as a function of oxidation temperature and time, corrected for the amount of oxide formed during the heating and cooling periods (Paper V).**

These results suggest that more reactions proceed in parallel during oxidation. At lower temperatures (473-673 K), a reaction with low activation energy dominates. The observed saturation to low oxide content is explained with a limited amount of the reactive sites on the pore walls. At higher temperatures (873-1073 K), other reactions with higher activation energies are enabled, because of the high thermal energy of the reactants. Similar results were found for samples of ~83% porosity. Nevertheless, due to the higher specific surface area with more high-energy reaction centers on the surface, oxidation is faster and shows higher saturation for lower temperatures, compared to the 70% porosity samples.

In order to determine the chemical reaction kinetics of oxidation, general reaction kinetic solutions of different-order reactions (first- and second- as well as third-order) were fitted to the experimental results (Atkins 2002). The first-order kinetics showed the best fits to the  $ox^*(T,t)$  data as

$$ox^* = 1 - e^{-kt} . \quad (21)$$

The fitting parameter  $k$  defines the reaction rate coefficients of chemical reactions at given temperatures. By plotting  $\ln k$  as a function of  $-(1/RT)$ , one can obtain (Fig. 21) the activation energy ( $E_a$ ) and the collision rate ( $A$ ) of the reactions from the Arrhenius law,

$$k = A \cdot e^{-E_a/RT} . \quad (22)$$

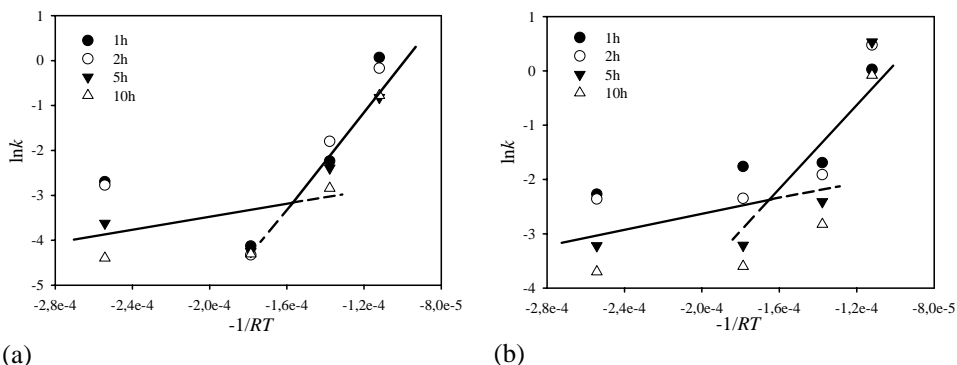


**Fig. 22. Arrhenius plots of thermal oxidation reaction rates of PS with porosities (a) 70% and (b) 83% (Paper V).**

The nonlinearity of the Arrhenius plots supports the presumption concerning the presence of two types of oxidation mechanisms. Therefore, two linear functions were fitted to both graphs (Fig. 22), one over the points representing the temperatures 473, 673 and 873 K, and the other for 673, 873 and 1073 K. The obtained slopes give the activation energies and collision numbers for the reactions occurring at a given temperature range (Table 6).

*Table 6. Activation energies of the reactions (Paper V).*

Porosity	$E_{a,1}$ (kJ/mol)	$E_{a,2}$ (kJ/mol)
70%	$8.3 \pm 3.5$	$55.1 \pm 6.3$
83%	$5.4 \pm 1.4$	$44.6 \pm 7.2$

The activation energy of oxidation is lower for the higher porosity samples in both reactions. This might be due to a higher stress formed in the higher porosity membranes, which is known to enhance oxidation for most metals (Nánai *et al.* 1992). Due to the large deviation of the pre-exponential constants, it was not possible to find any characteristic variation of the collision rate with the porosity. For both porosities, the average collision numbers were  $\sim 0.2$  and  $\sim 100 \text{ h}^{-1}$  for the reactions with lower and higher activation energies, respectively.

The reaction with low activation energy and collision number represents the oxidation of the pore walls. This is the reaction path which is probably most responsible for the aging of PS layers stored in air. It is known that the H original impurity desorbs from the surface when annealed at 573-773 K. Below that temperature range, the oxidation is probably limited by the H passivation layer, which might be a reason for the low collision rate obtained for low temperature oxidation. The second reaction, with considerably higher activation energy, is related to the oxidation of the bulk of the Si skeleton. In this case, the increased activation energy is due to the additional energy needed for the diffusion of oxygen through the oxide layer toward the Si-SiO<sub>2</sub> interface.

## 4.3 Some applications of porous silicon

### 4.3.1 *Optical applications*

Several potential applications of PS have been investigated and realized in various fields (Table 3). In Chapter 4.1, Bragg gratings have been demonstrated.

Periodic structures of PS act as Bragg filters (Paper II). By considering the proper Bragg conditions, the fabrication of optical filter or reflector components can be performed in a simple manner. The reflection bands can be set from ~700 nm up to few microns by tuning etching times and current densities. The application in IR is extremely easy due to the very low absorption coefficient. When a reflector is used in shorter wavelength applications, higher porosity layers are favorable, because the optical absorption close to the visible range can be decreased by increased porosity. The reflectivity of mirrors/filters can be increased by stacking more alternating layers. In IR, due to the very low absorption coefficient, the thickness of the structure and thus the number of layers is not a limiting factor. Nevertheless, below 800 nm, the reduction of total thickness is appropriate because of the strong absorption. Therefore, application of less layers having large difference in their refractive indices is recommended.

Moreover, the reflected light intensity by the Bragg filter is strongly dependent on the refractive index of the ambient medium. If the pores of multilayer stacks are filled with a medium having different refractive index than that of vacuum or air, the position and width of the reflection bands change. Due to the effect of the pore-filling medium on the optical properties of the porous Bragg filters, the Bragg condition of the stack can be tuned by introducing a proper medium into the pores. This effect is exploited in optical-chemical sensing (Mulloni & Pavesi 2000) or in chemical-optical actuators, such as mirrors and filters, controlled by the composition or concentration of the ambient medium.

Anti-reflection coatings were created on PS layers by gradually increasing the anodization current density from the processing value up to the current density needed for electropolishing in the given electrolyte (Paper III). Layers with reflections below 1% were obtained in the 700-1700 nm range.

### 4.3.2 *Carbon nanotube synthesis on porous silicon*

It is a challenging task to integrate CNTs into a Si environment and to find selective synthesis methods which are compatible with standard silicon processing. Both PS and CNTs are considered as new alternative building blocks in future nanoelectronic, field emission, photonic and nano-sensor devices. In this study, the effect of oxidation extent of PS substrates on the catalytic CVD growth of CNTs was investigated (Paper VI). It is found that the CNT growth is advanced on oxidized PS surfaces (Fig. 23), which is explained by the diffusion barrier effect of SiO<sub>2</sub>.

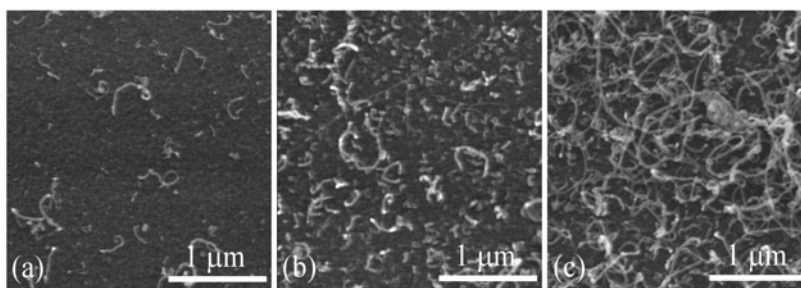


**Fig. 23. CCVD growth of CNTs on (a) pristine and oxidized PS surface at (b)673 K and (c) 1073 K (Paper VI).**

Catalytic Fe nanoparticles are chemically stable on the surface of  $\text{SiO}_2$ , thus remaining active during the CVD process. On the Si surface, Fe reacts with the substrate, yielding a catalytically-inactive  $\text{FeSi}_2$  phase. Therefore, the poisoning of the catalyst, as well as the outcome of the catalytic CVD process, depends on the diffusion rate of the Fe towards Si through the  $\text{SiO}_2$  layer.

From the results of TEM analyses, it was observed that neither Fe particles nor CNTs are inside the pores. The ferrocene molecules decompose before infiltrating the holes of PS, so that Fe deposition occurs only on the outer surfaces of the substrates.

The formed tubes are irregular and curved due to the inclusion of dislocation in the walls. The reason for asymmetric growth can be associated with (i) composition inhomogeneity due to the impurities built in the catalyst, (ii) effect of the porous non-uniform substrate, (iii) irregular shapes of catalyst, and (iv) for crystalline catalysts the difference in the physical-chemical properties among the crystal faces. The large number of the catalytic nanoparticles trapped in the inner cavity of the tubes suggests a base-growth mechanism with periodic detachment of the catalyst from the substrate during the growth period. The closed and empty free tube ends found for most of the tubes also support this mechanism (Fig. 24).

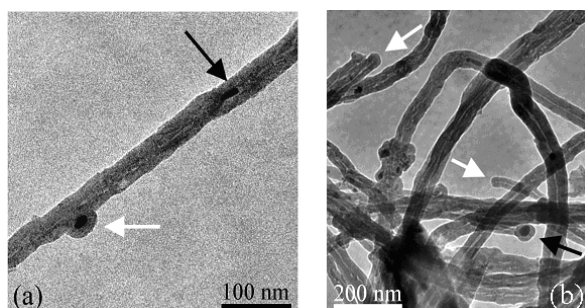
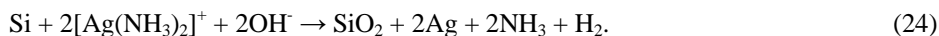
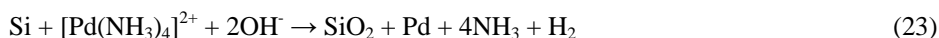


**Fig. 24. TEM images of (a) catalytic nanoparticles inside (black narrow) and on the surface of CNT (white narrow), and (b) the closed empty tube free ends MWCNT (white narrow). The empty ends suggest a base-growth mechanism, and the filled ends (black narrow) one an indication of a tip-growth mechanism (Paper VI).**

### 4.3.3 Silver and palladium deposition on porous silicon for a novel catalyst

Due to the high specific surface area and high electronegativity, PS is an effective reducing surface. Metals such as Pt, Pd, Ag and Ni play an important role in heterogeneous chemical catalysis, especially when these materials are present in the form of small sub-micron size seeds or crystallites. The combination of these metals with PS could provide novel catalyst substrates, where Pd and Ag were deposited on PS from liquid phase precursors using the immersion plating method (Paper VII).

As the electrolyte infiltrates the pores of the spongy structure, the metal ions are reduced into neutral metals by the surface of the pores. The PS acts as an electron donor, thus reducing the palladium and silver ions in alkaline media, while SiO<sub>2</sub>, Pd/Ag and hydrogen form. Considering the reactants and products, the following reactions can be proposed for the immersion plating:



The role of the reactant concentrations in the deposition process was investigated. It was observed in the FESEM images that the higher [Ag(NH<sub>3</sub>)<sub>2</sub>]<sup>+</sup> concentration results in the formation of large Ag seeds on top of the PS surface. The size of the Ag grain decreased with lower concentration, and meanwhile, a three-dimensional porous Ag network formed on the substrate (Fig. 25). However, the Pd seeds are much smaller than those of Ag, and the Pd seed size did not show variation with the concentration of [Pd(NH<sub>3</sub>)<sub>4</sub>]<sup>2+</sup>. Moreover, traces of Ag-Pd alloy crystallites were not found by the FESEM/EDX analysis, i.e., all the deposited particles were individual seeds of Ag and Pd.

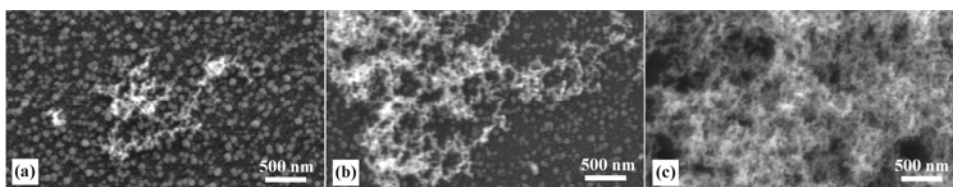


**Fig. 25.** Three-dimensional Ag structures grown on PS after 10 s immersion plating in electrolytes of: (a) 0.008 M AgNO<sub>3</sub>, 0.002 M Pd(ac)<sub>2</sub>, 0.4 M NH<sub>4</sub>OH, (b) 0.0066 M AgNO<sub>3</sub>, 0.0033 M Pd(ac)<sub>2</sub>, 0.4 M NH<sub>4</sub>OH and (c) 0.005 M AgNO<sub>3</sub>, 0.005 M Pd(ac)<sub>2</sub>, 0.4 M NH<sub>4</sub>OH (Paper VII).

Further investigations of the metal deposition were carried out using TEM/EDX, and the results were in agreement with the previous FESEM/EDX analyses: alloy or agglomerated crystal form of the deposited Ag and Pd were not present. The pores of the structure were partly filled with large (50-100 nm) Ag and smaller (1-40 nm) Pd seeds (Fig. 26).

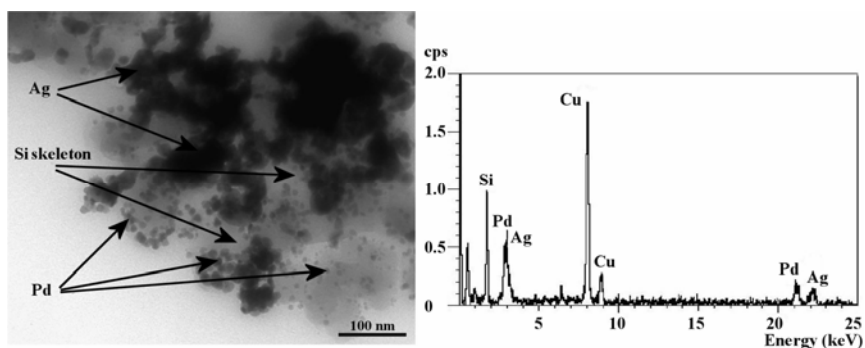


**Fig. 26.** TEM image and EDX spectrum of metallized PS sample (120 s plating in 0.002 M  $\text{AgNO}_3$ , 0.008 M  $\text{Pd}(\text{ac})_2$ , 0.4 M  $\text{NH}_4\text{OH}$ ). The deposits are individual seeds of Ag and Pd embedded in the pores of the Si skeleton. Peaks of Cu  $K\alpha$  and Cu  $K\beta$  rise from the sample holder copper grid (Paper VII).

The samples were studied also with XRD. Due to the very small size of the individual Ag and Pd seeds, diffraction peaks were not found. In order to create larger and crystallized particles, the metallized samples were annealed. FESEM/EDX analyses revealed that significant changes at 523 K did not happen, and at 773 and 1023 K the average metal grain size became larger, and some of the Ag and Pd seeds were oxidized. XRD measurements have been repeated on the annealed samples, and the results have corroborated the FESEM observation. Recrystallization or agglomeration of both metals after annealing at 773 and 1023 K was concluded from the appearance of the (111) and (200) peaks. Samples treated at 1023 K gave  $\text{Ag}_2\text{O}$  and  $\text{PdO}$  peaks besides the metal peaks, but peaks of the Ag-Pd alloy phase were not found for any samples. Furthermore, the PS structure became partly oxidized.

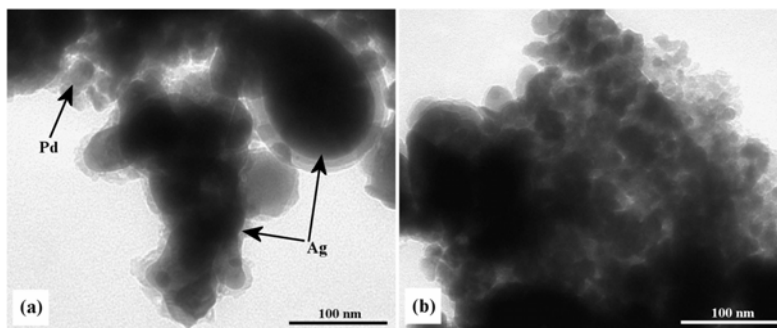


**Fig. 27.** TEM images and EDX spectrum of the metallized PS (120 s plating in 0.002 M  $\text{AgNO}_3$ , 0.008 M  $\text{Pd}(\text{ac})_2$ , 0.4 M  $\text{NH}_4\text{OH}$ ) after annealing at 773 K. (a) Large Ag seeds with oxide shell and same Pd grains can be seen. (b) Pd agglomerates (Paper VII).

Investigations by TEM/EDX also revealed a slight re-crystallization and partial oxidation of both metals at 773 and 1023 K (Fig. 26). The TEM/EDX analysis performed on

individual grains confirmed the results obtained by XRD. Alloyed Ag-Pd particles were not found, where the seeds were either palladium or silver.

## 5 Conclusions

Synthesis, investigation, properties and some selected application of pristine and oxidized porous silicon structures are discussed in this thesis. PS layers having different thickness and porosity were prepared and analyzed. The dependence of the thickness on the anodization time and the effect of current density and electrolyte composition on the porosity were determined and found proportional within a good range. The optical properties of well-defined structures (thickness and porosity) were calculated using the envelope method, Fresnel's equation, the rules of optical interference and Bruggeman's EMA. Optical transmission and reflection spectra of freestanding PS films were recorded, and the refractive indices and absorption coefficients were calculated. A comparative study on the optical properties determined from experimental and theoretical approaches showed that light scattering takes place at the air-PS interface in the measured range. Due to the presence of photon scattering, the optical parameters cannot be derived precisely from the transmission spectra using the envelope method. It is because the scattering causes light intensity loss, and the envelope functions in the transmission spectrum cannot open up properly. Based on optical reflection measurements, similar results were found. Since the relative position of the extrema of oscillations in the transmitted light spectrum are fairly independent of the scattering losses, the index of refraction can be calculated by considering the conditions of optical interference. The calculated refractive indices agree well with the EMA in the applied wavelength range 700-1700 nm.

Based on the results obtained from the investigations of PS structures (manufacturing conditions and those effects on the optical properties), multilayer PS stacks were designed, fabricated and studied. The recorded optical transmission spectra of the reflectors showed good matching with the calculations. The investigated Bragg mirrors proved to be excellent reflectors in the near-IR wavelength range.

The spontaneous oxidation of the PS structure is a disadvantage in the applications of the PS layers. This aging effect can be eliminated by partial or full oxidation of the porous material. Since dry thermal oxidation in normal air of PS seemed to be one of the most plausible methods, it was investigated from different aspects. It is found that PS samples can be oxidized rapidly in air at moderate temperatures (473-1073 K), and the grown oxide is a result of two different oxidation reactions both having first-order reaction kinetics. The structure of oxidized membranes was studied using a number of

different techniques. The grown oxide was found amorphous. As revealed, stress arises in the residual Si skeleton during oxidation, which results in the deformation of crystal lattice.

The PS technology provides extremely good flexibility in the realization of various optical devices. In this thesis, Bragg filters and anti-reflection coatings as optical applications of PS structures have been demonstrated.

The combination of PS and CNT networks promises good potential for future nanoelectronic, field emission, photonic and nano-sensor devices. Therefore, the synthesis of CNT networks on various PS substrates was studied. It was found that, similar to the bulk Si/SiO<sub>2</sub> system, the increase of the oxide layer thickness on the PS pore walls enhances the CNT growth yield.

Due to the high specific surface area and reducing behavior, PS enables the chemical reduction of metal ions/complexes. Since Pd and Ag play important roles in heterogeneous catalysis, it was decided to deposit both metals and their alloys on PS. As revealed, individual nanoparticles of Pd and Ag can be deposited in the pores of PS using the immersion plating technique. Co-deposition of Pd and Ag was not obtained.

As a summary, the following new scientific results having potential in future applications of PS are:

- Wavelength-dependent refractive indices of freestanding PS membranes in 700-1700 nm range for samples of different porosities.
- Validation of Bruggeman's effective medium theory for PS.
- Presence of photon scattering at the air-PS interface and its limiting effect on the validity of the envelope method.
- Reaction kinetics parameters of dry thermal oxidation in air.
- Strain in the residual Si skeleton after partial oxidation due to the intrinsic stresses and thermal expansion coefficient mismatch between the amorphous SiO<sub>2</sub> and crystalline Si phases in the porous layer.
- Effect of the oxidation extent of PS on the suitability for MWCNT growth by CCVD.
- Demonstration of the suitability of PS for the synthesis of Pd and Ag nanoparticles by the immersion plating method.

## References

- Ádám M, Horváth ZsJ, Bársony I, Szölgvényi L, Vázsonyi E & Tuyen VV (1995) Investigation of electrical properties of Au/porous Si/Si structures. *Thin Solid Films* 255: 266-268.
- Aroutiounian VM, Martirosyan K & Soukissian P (2004) Low reflectance of diamond-like carbon/porous silicon double layer antireflection coating for silicon solar cells. *J. Phys. D* 37 (19): L25-L28.
- Arrand HF (1997) Optical waveguides and components based on porous silicon. PhD thesis, University of Nottingham, UK: 63-66.
- Astrova EV, Ratnikov VV, Remenyuk AD & Shul'pina IL (2002) Starins and crystal lattice defects arising in macroporous silicon under oxidation. *Semiconductors* 36: 1033-1042.
- Astrova EV, Voronkov VB, Remenyuk AD & Shuman VB (1999) Variation of the parameters and composition of thin films of porous silicon as a result of oxidation: ellipsometric studies. *Semiconductors* 33 (10): 1149-1155.
- Atkins PW & de Paula J (2002) *Physical chemistry*. Oxford University Press, Oxford, UK.
- Balucani M, Bondarenko V, Klusko A & Ferrari A (2005) Recent progress in integrated waveguides based on oxidized porous silicon. *Opt. Mat.* 27 (5): 776-780.
- Barla K, Herino R, Bomchil G, Pfiser JC & Freund A (1984) Determination of lattice parameter and elastic properties of porous silicon by X-ray diffraction. *J. Cryst. Growth* 68 (3): 727-732.
- Beckmann KH (1965) Investigation of the chemical properties of stain films on silicon by means of infrared spectroscopy. *Surface Science* 3: 314-332.
- von Behren J & Fauchet PM (1997) Absorption coefficient of porous silicon. In: Canham L (ed) *Properties of porous silicon*. INSPEC, London: 229-233.
- Bellet D (1997) Drying of porous silicon. In: Canham L (ed) *Properties of porous silicon*. INSPEC, London: 38-43 and 127-131.
- Ben-Chroin M (1997) Resistivity of porous silicon. In: Canham L (ed) *Properties of porous silicon*. INSPEC, London: 38-43 and 165-175.
- Bisi O, Ossicini S & Pavesi L (2000) Porous silicon: a quantum sponge structure for silicon based optoelectronics. *Surface Science Rep.* 38: 1-126.
- Bondarenko VP & Yakovtseva VA (1997) Microelectronic applications of porous silicon. In: Canham L (ed) *Properties of porous silicon*. INSPEC, London: 343-348.
- Bondarenko VP & Yakovtseva VA (1997) Optoelectronic applications of porous silicon. In: Canham L (ed) *Properties of porous silicon*. INSPEC, London: 356-363.
- Bratkowski A, Korcala A, Lukasiak Z, Borowski P & Bala W (2005) Novel gas sensor based on porous silicon measured by photovoltage, photoluminescence, and admittance spectroscopy. *Opto-Electronics Review* 13 (1): 35-38.

- Bruggeman DAG (1935) Berechnung verschiedener physikalischer Konstanten von heterogen Substanzen. *Ann. Phys. (Leipzig)* 24: 636-679.
- Bsiesy A (1997) Electroluminescence from porous silicon using liquid contacts. In: Canham L (ed) *Properties of porous silicon*. INSPEC, London: 283-289.
- Chan S, Horner SR, Fauchet M & Miller BL (2001) Identification of gram negative bacteria using nanoscale silicon microcavities. *J. Am. Chem. Soc.* 123 (47): 11797-11798.
- Canham LT (1990) Silicon quantum wire array fabrication by electrochemical and chemical dissolution of wafers. *Appl. Phys. Lett.* 57: 1046-1048.
- Canham LT (1997) Storage of porous silicon. In: Canham L (ed) *Properties of porous silicon*. INSPEC, London: 44-50.
- Canham LT (1997) Visible photoluminescence from porous silicon. In: Canham L (ed) *Properties of porous silicon*. INSPEC, London: 249-255.
- Canham LT (1997) Biomedical applications of porous silicon. In: Canham L (ed) *Properties of porous silicon*. INSPEC, London: 371-376.
- Canham LT, Houlton MR, Leong WY, Pickering C & Keen JM (1991) Atmospheric impregnation of porous silicon at room temperature. *J. Appl. Phys.* 70 (1): 422-431.
- Cox TI (1997) Porous silicon layer capacitance. In: Canham L (ed) *Properties of porous silicon*. INSPEC, London: 185-191.
- Cox TI (1997) Electroluminescence from porous silicon using solid state contacts. In: Canham L (ed) *Properties of porous silicon*. INSPEC, London: 290-310.
- Cullis AG, Canham LT & Calcott PDJ (1997) The structural and luminescence properties of porous silicon. *J. Appl. Phys.* 82 (3): 909-965.
- DeLouise LA & Miller BL (2004) Quantitative assessment of enzyme immobilization capacity in porous silicon. *Anal. Chem.* 76 (23): 6915-6920.
- Duttagupta SP, Chen XL, Jenekhe SA & Fauchet PM (1997) Microhardness of porous silicon films and composites. *Solid State Comm.* 101 (1): 33-37.
- Dzhafarov TD, Oruc C & Aydin S (2004) Humidity-voltaic characteristics of Au - porous silicon interfaces. *J. Phys. D* 37: 404-408.
- Edmund catalog (2004) *Optics and optical instruments catalog*. Edmund Optics Ltd: p. 98.
- Françon F (1966) *Optical interferometry*. Academic Press, New York: 105.
- Franssila S (2004) *Introduction to microfabrication*. John Wiley & Sons Ltd. UK: 123-125.
- Fried M, Lohner T, Polgár O, Petrik P, Vázsonyi É, Bársony I, Piel JP & Stehle JL (1996) Characterization of different porous silicon structures by spectroscopic ellipsometry. *Thin Solid Films* 276: 223-227.
- Garnett JCM (1904) Colours in metal glasses and in metallic films. *Phil. Trans. R. Soc. (London)* 203: 385-420.
- Goryachev DN, Belyakov LV & Sreseli OM (2000) On the mechanism of porous silicon formation. *Semiconductors* 34(9): 1090-1093.
- Grosman A & Ortega C (1997) Chemical composition of 'fresh' porous silicon. In: Canham L (ed) *Properties of porous silicon*. INSPEC, London: 145-153.
- Halimaoui A, Oules C, Bomchill G, Bsiesy A, Gaspard F, Herino R, Ligeon M & Muller F (1991) Electroluminescence in the visible range during anodic oxidation of porous silicon films. *Appl. Phys. Lett.* 59 (3): 304-306.
- Halimaoui A (1997) Porous silicon formation by anodisation. In: Canham L (ed) *Properties of porous silicon*. INSPEC, London: 12-14.
- Harrison HB & Dimitriev S (1991) Ultr-thin dielectrics for semiconductor applications – growth and characteristics. *Micrel. J.* 3-38.
- Hawkes J & Latimer I (1995) *Lasers: Theory and practice*. Prentice Hall, Europe: 222-.
- Hérino R (1997) Pore size distribution in porous silicon. In: Canham L (ed) *Properties of porous silicon*. INSPEC, London: 89-96.

- Hilliard J, Andsager D, Hassan LA, Nayfeh HM & Nayfeh MH (1994) Infrared spectroscopy and secondary ion mass spectrometry of luminescent, nonluminescent, and metal quenched porous silicon. *J. Appl. Phys.* 76 (4): 2423-2428
- Hossain SM, Chakraborty S, Dutta SK, Das J & Saha H (2000) Stability in photoluminescence of porous silicon. *J. Lumin.* 91: 195-202.
- Ito T, Yamama A, Hiraki A & Satou M (1989) Silicidation of porous silicon and its application for the fabrication of a buried metal layer. *Appl. Surf. Sci.* 41-42: 301-305.
- Karacali T, Cakmak B & Efeoglu H (2003) Aging of porous silicon and the origin of blue shift. *Optics Express* 11: 1237-1242.
- Kolasinski KW (2003) The mechanism of Si etching in fluoride solutions. *Phys. Chem. Chem. Phys.* 5: 1270-1278.
- Kooij ES & Kelly LL (1997) Chemiluminescence from porous silicon. In: Canham L (ed) *Properties of porous silicon*. INSPEC, London: 276-279.
- Lang W (1997) Thermal conductivity of porous silicon. In: Canham L (ed) *Properties of porous silicon*. INSPEC, London: 128-141.
- Lang W (1997) Micromachining applications of porous silicon. In: Canham L (ed) *Properties of porous silicon*. INSPEC, London: 377-383.
- Lehmann V (1997) A new capacitor technology based on porous silicon. In: Canham L (ed) *Properties of porous silicon*. INSPEC, London: 390-396.
- Lehmann V & Gösele U (1991) Porous silicon formation: A quantum wire effect. *Appl. Phys. Lett.* 58 (8): 856-858.
- Lehmann V, Jobst B, Muschik T, Kux A & Petrova-Koch V (1993) Correlation between optical properties and crystallite size in porous silicon. *Jpn. J. Appl. Phys.* 32: 2095-2099.
- Looyenga H (1965) Dielectric constants of heterogeneous mixtures. *Physica* 31: 401-406.
- Maiello G, Monica SL, Ferrari A, Masini G, Bondarenko VP, Dorofeev AM & Kazuchits NM (1997) Light guiding in oxidized porous silicon optical waveguides. *Thin Solid Films* 297: 31113.
- Manificier JC, Gasiot J & Fillard JP (1976) A simple method for the determination of the optical constants  $n$ ,  $k$  and the thickness of a weakly absorbing thin film. *J. Phys. E* 9: 1002-1004.
- Menna P & Tsuo S (1997) Solar cells using porous silicon. In: Canham L (ed) *Properties of porous silicon*. INSPEC, London: 384-389.
- Mizsei J, Shrair JA & Zólogy I (2004) Investigation of Fermi-level pinning at silicon/porous-silicon interface by vibrating capacitor and surface photovoltage measurements. *Appl. Surf. Sci.* 235: 376-388.
- Mulloni V & Pavesi L (2000) Porous silicon microcavities as optical chemical sensors. *Appl. Phys. Lett.* 76 (18): 2523-2525.
- Nakajima Y, Uchida T, Toyama H, Kojima A, Gelloz B & Koshida N (2004) A solid-state multicolor light-emitting device based on ballistic electron excitation. *Jap. J. Appl. Phys. Part 1* 43 (4B): 2076-2079.
- Nánai L, Vajtai R, Hevesi I, Laiho R & Heikkala L (1992) Periodic nanostructures observed by STM on vanadium surface preilluminated with a cw Yag-laser. *Superlattices and Microstructures* 11 (4): 435-438.
- Parkhutik V (1999) Porous silicon – mechanism of growth and applications. *Solid-state Electron.* 43: 1121-1141.
- Petit D, Chazalviel JN, Ozanam F & Devreux F (1997) Porous silicon structure studied by nuclear magnetic resonance. *Appl. Phys. Lett.* 70 (2): 191-193.
- Petrova EA, Bogoslovskaya KN, Balagurov LA & Kochoradze GI (2000) Room temperature oxidation of porous silicon in air. *Mater. Sci. Eng. B* 69-70: 152-156.
- Qin GG & Lin J (1997) Ultraviolet photoluminescence from porous silicon. In: Canham L (ed) *Properties of porous silicon*. INSPEC, London: 264-269.

- Ottow S (2005) Basics of semiconductor electrochemistry. <http://www.techfak.uni-kiel.de/matwis/amat/poren/ecintro.html>.
- Pickering C, Beale MIJ, Robbins DJ, Pearson PJ & Greef R (1984) Optical studies of the structure of porous silicon films formed in p-type degenerate and non-degenerate silicon. *J. Phys. C* 17: 6535-6552.
- Pramanik C, Islam H & Saha H (2005) Design, fabrication, testing and simulation of porous silicon based smart MEMS pressure sensor. *IEEE Computer Society, 18<sup>th</sup> International Conference on VLSI'05*: 235-240.
- Rajamaran S & Henderson HT (2005) A unique fabrication for microneedles using coherent porous silicon technology. *Sensors and Act. B* 105 (2): 443-448.
- Read AJ, Needs RJ, Nash KJ, Canham LT, Calcott PDJ & Qteish A (1992) First-principles calculation of the electronic properties of silicon quantum wires. *Phys. Rev. Lett.* 69 (8): 1232-1235.
- Rossi AM, Amato G, Camarchia V, Boarnio L and Borini S (2001) High-quality porous-silicon buried waveguides. *Appl. Phys. Lett.* 78 (20): 3003-3005.
- Sailor MJ (1997) Sensor applications of porous silicon. In: Canham L (ed) *Properties of porous silicon*. INSPEC, London: 364-370.
- Sauer R (1997) Near infrared photoluminescence from porous silicon. In: Canham L (ed) *Properties of porous silicon*. INSPEC, London: 256-263.
- Smith RL & Collins SD (1992) Porous silicon formation mechanisms. *J. Appl. Phys.* 71 (8): R1-R22.
- Snow PA, Squire EK, Russel PStJ and Canham LT (1999) Vapor sensing using the optical properties of porous silicon Bragg mirrors. *J. Appl. Phys.* 86 (4): 1781-1784.
- Solanki CS, Carnel L, Van Nieuwenhuysen K, Ulliyashin A, Posthuma N, Beaucarna G & Poortmans J (2005) Thin-film free-standing monocrystalline Si solar cells with heterojunction emitter. *Progress in Photovolt.* 13 (3): 201-208.
- Streetman BG & Banerjee S (2000) Energy bands and charge carriers in semiconductors. In: Streetman BG & Banerjee S (eds) *Solid state electronics devices*. Prince Hall, Inc. New Jersey: 55-107.
- Streetman BG & Banerjee S (2000) Junctions. In: Streetman BG & Banerjee S (eds) *Solid state electronics devices*. Prince Hall, Inc. New Jersey: 142-240.
- Takai H & Itoh T (1986) Porous silicon layers and its oxide for the silicon-on-insulator structure. *J. Appl. Phys.* 60: 222-225.
- Theiß W (1997) Optical properties of porous silicon. *Surf. Sci. Rep.* 29: 91-192.
- Theiß W & Hilbrich S (1997) Refractive index of porous silicon. In: Canham L (ed) *Properties of porous silicon*. INSPEC, London: 223-228.
- Thönissen M, Krüger M, Lerondel G & Romstain R (1997) Optical applications of porous silicon. In: Canham L (ed) *Properties of porous silicon*. INSPEC, London: 349-355.
- Timoshenko VY, Dittrich T, Lysenko V, Lisachenko MG & Koch F (2001) Free charge carriers in mesoporous silicon. *Phys. Rev. B* 64: 085314-1-8.
- Tóth G, Kordás K, Pap AE, Vähäkangas J, Uusimäki A & Leppävuori S (2005) Origin and FEM-assisted evaluation of residual stress in thermally oxidized porous silicon. *Comp. Mater. Sci.* 34 (2): 123-128.
- Uhlir A (1965) Electrolytic shaping of germanium and silicon. *Bell Syst. Tech. J.* 35: 333-347.
- Vázsonyi ÉB, Koós M, Jalsovzsky G & Pócsik I (1993) The role of hydrogen in luminescence of electrochemically oxidized porous Si layer. *J. Lumin.* 57: 121-124.
- Vinegoni C, Cazzanelli M & Pavesi L (2001) Porous silicon microcavities. In: Nalwa HS (ed.) *Silicon based materials and devices volume 2: Properties and devices*. Academica Press HSTC, USA: 123-192.

- Volk J, Balazs J, Toth AL & Barsony I (2004) Porous silicon multilayers for sensing by tuneable IR-transmission filtering. *Sensors and Actuators B* 100 (1-2): 163-167.
- Williams GM (1997) Cathodoluminescence properties of porous silicon. In: Canham L (ed) *Properties of porous silicon*. INSPEC, London: 270-275.
- Watanabe Y & Sakai T (1971) Application of a thick avoided film to semiconductor devices. *Rev. Electron. Commun. Labs.* 19: 899-903.
- Yablonovitch E, Allara DL, Chang CC, Gmitter T & Bright TB (1986) Unusually low surface-recombination velocity on silicon and germanium surfaces. *Phys. Rev. Lett.* 57 (2): 249-252.
- Yamazaki Y (2004) Application of MEMS technology to micro fuel cells. *Electrochimica Acta* 50 (2-3) 663-666.
- Yonahara T (1997) BESOI with porous silicon: ELTRAN<sup>®</sup>. In: Canham L (ed) *Properties of porous silicon*. INSPEC, London: 397-399.